

Waveguide QED at the onset of spin-spin correlations

Sebastián Roca-Jerat,¹ Marcos Rubín-Osanz,¹ Mark D. Jenkins,¹
Agustín Camón,¹ Pablo J. Alonso,¹ David Zueco,¹ and Fernando Luis¹

¹*Instituto de Nanociencia y Materiales de Aragón (INMA),
CSIC-Universidad de Zaragoza, Zaragoza 50009, Spain*

We experimentally explore the competition between light-mediated and direct matter-matter interactions in waveguide quantum electrodynamics. For this, we couple a superconducting line to a model magnetic material, made of organic free radical DPPH molecules with a spin $S = 1/2$ and a g_S factor very close to that of a free electron. The microwave transmission has been measured in a wide range of temperatures ($0.013 \text{ K} \leq T \leq 2 \text{ K}$), magnetic fields ($0 \leq B \leq 0.5 \text{ T}$) and frequencies ($0 \leq \omega/2\pi \leq 14 \text{ GHz}$). We find that molecules belonging to the crystal sublattice B form one-dimensional spin chains. Temperature then controls intrinsic spin correlations along the chain in a continuous and monotonic way. In the paramagnetic region ($T > 0.7 \text{ K}$), the microwave transmission shows evidences for the collective coupling of quasi-identical spins to the propagating photons, with coupling strengths that reach values close to the dissipation rates. As T decreases, the growth of intrinsic spin correlations, combined with the anisotropy in the spin-spin exchange constants, break down the collective spin-photon coupling. In this regime, the temperature dependence of the spin resonance visibility reflects the change in the nature of the dominant spin excitations, from single spin flips to bosonic magnons, which is brought about by the magnetic correlation growth.

The interaction of N quantum emitters with electromagnetic radiation fundamentally differs from the mere superposition of the individual emitter couplings. The collective nature of this interaction manifests itself in an enhanced superradiant light emission and in the broadening of the absorption lines [1, 2]. The underlying mechanism is the light-mediated interaction among emitters, leading to the formation of collective Dicke states [3, 4]. In free space, light-matter coupling is very weak, thus such effects are hard to detect unless photons are confined. In cavity Quantum Electrodynamics (QED), the electromagnetic radiation is confined in all spatial dimensions [5], such that emitters interact with a discrete set of photon cavity modes. In *waveguide* QED (wQED), matter interacts with photons propagating along the guide, which form a continuous spectrum. Recent experimental realizations of wQED span the optical to microwave regimes, incorporating real or artificial atoms and various material supports for the waveguides [6–20].

So far, in wQED the focus has been mainly on otherwise quasi-independent emitters, where all interactions occur through photons. On-chip resonators and transmission lines have also been used to measure the excitation spectra of systems showing intrinsic order, e.g. in layered magnetic materials [24, 25]. In this case, spin excitations are also collective states, but correlations are dominated by interactions inherent to the material. Exploring situations in which the two effects compete remains virtually uncharted. Yet, there are compelling reasons to consider them. Firstly, because the close packing of emitters unavoidably generates interactions among them [26–28]. And secondly, because their different signs and ranges can introduce ways to tune the order and thus create novel states [29–31].

In this work, we experimentally address the competition between light-mediated and intrinsic spin-spin interactions in a magnetic material coupled to microwave photons propagating via a superconducting transmission line (Fig. 1a). We focus on a particular model system, an organic free radical, in which spin-spin correlations grow along 1D chains [32] and can, therefore, be gradually controlled by either changing temperature or magnetic field. The broadband nature of the waveguide helps overcoming the limitations associated with narrow band in cavity QED [25, 32–34], albeit at the price of a weaker spin-photon coupling. In particular, it allows studying the spin excitations at different energy scales within a single experiment. Here, we exploit this characteristic to study how the photon transmission reflects changes in the nature and properties of such excitations.

All experiments described below used the 2,2-diphenyl-1-picrylhydrazyl (hereafter DPPH) organic free radical [21, 35] in powder form, as purchased from Sigma Aldrich. Even though solvent-free DPPH has been known for a long time [35], a full structural determination was not performed until quite recently [21]. X-ray diffraction experiments, shown in the accompanying Supplemental Material [36], suggest that this material exhibits the DPPH-III crystal structure [21] (Fig. 1a) that contains two inequivalent DPPH sites, referred to as A and B sublattices. Each DPPH radical hosts a spin $S = 1/2$ with a nearly isotropic $g_S \simeq 2.004$ factor. At either high temperatures T or in a sufficiently diluted form, it behaves as a model ensemble of quasi-identical, paramagnetic moments. On the other hand, in dense materials and for sufficiently low T , interactions between neighbour radicals become relevant [21, 32, 37, 38].

The magnetic response of DPPH has been studied via a

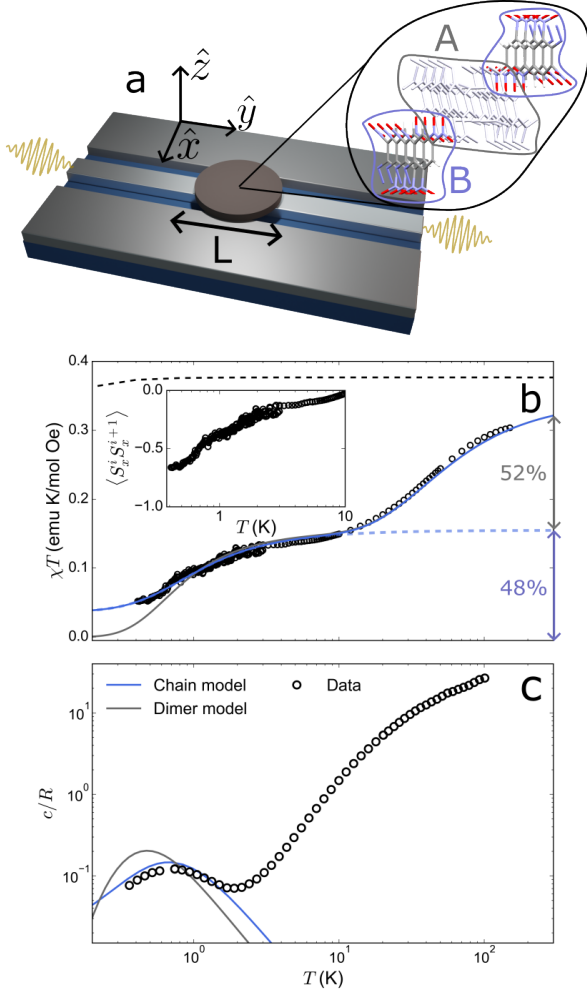


FIG. 1. (a) Sketch of the setup used in transmission experiments, showing an image of the two molecular subspecies, A and B, present in the DPPH crystal structure [21]. (b) Product of the magnetic susceptibility χ times temperature, measured on a powdered DPPH sample from 0.3 K up to 100 K and for $B = 0.1$ T. The blue (grey) solid line is a fit with a model that considers the formation of antiferromagnetic dimers within sublattice A and then of spin chains (dimers) within sublattice B, as T decreases. The inset shows the correlation function between nearest neighbour spins estimated as $\langle S_i^x S_{i+1}^x \rangle \simeq -[1 - \chi T / C_B]$ [22, 23], where $C_B = 0.1536$ emu K/mol Oe is the Curie constant of the B-type DPPH molecules. (c) Specific heat of DPPH measured from 0.3 K to 100 K at $B = 0$. The blue (grey) solid line are results calculated with the chain [22] (dimer [21]) model for the magnetic contribution of spins in sub-lattice B.

combination of magnetic susceptibility and specific heat experiments performed for $0.3 \leq T \leq 100$ K. The results are shown in Fig. 1 and described in detail in [36]. The main conclusions are: *i*) a fraction, approximately 15 %, of DPPH molecules are in their oxidized form, which has $S = 0$; *ii*) molecules belonging to the A crystal sublattice form antiferromagnetic (AF) dimers, also with an $S = 0$ ground state, at relatively high temperatures $\lesssim 50$

K, and *iii*) DPPH spins in sublattice B form 1D chains along which AF correlations grow continuously as temperature decreases (see the inset of Fig. 1b). Below 10 K, only B-type molecules remain paramagnetic, albeit interacting along chains, and can therefore couple to microwave photons.

Microwave transmission experiments were performed with on-chip superconducting coplanar waveguides fabricated by optical lithography on a 100 nm Nb thin film deposited onto crystalline sapphire wafers. A 1 mm wide DPPH pellet was fixed on the 400 μ m wide central line by means of apiezon N grease. The transmission S_{21} through the central line was measured in the frequency range $10 \text{ MHz} \leq \omega/2\pi \leq 14 \text{ GHz}$ with a vector network analyzer. Since the sample size is smaller than the smallest photon wavelengths ($\lambda \geq 4.4 \text{ mm}$) we can disregard the dependence of the electromagnetic modes along the y axis of the device (cf Fig. 1a). A magnetic field $\vec{B} = B\hat{y}$, with $0 \leq B \leq 0.5$ T, was applied by a 9 T/1 T/1 T superconducting vector magnet. The chip was thermalized to the mixing chamber of a ^3He - ^4He dilution refrigerator giving access to the temperature region between 130 mK and 4.2 K. Additional experiments were performed with another dilution refrigerator with an even lower base temperature $\simeq 7$ mK. Then, \vec{B} was applied, also parallel to \hat{y} , by a 1 T axial superconducting magnet. In order to enhance the contrast of those effects associated with the coupling to the spins and compensate for the decay of S_{21} with increasing ω , S_{21} was normalized using data measured at two different magnetic fields, as described in [39, 40] and in [36].

We first examine S_{21} measured at $T = 2$ K, depicted in Fig. 2a. Transmission minima are observed when $\omega = \Omega \equiv g_S \mu_B B / \hbar$, indicating resonant absorption of photons by paramagnetic spins. The microwave transmission is interpreted through the light-matter Hamiltonian $\mathcal{H} = \mathcal{H}_M + \mathcal{H}_{WG} + \mathcal{H}_I$, which encompasses the spin system \mathcal{H}_M , the waveguide \mathcal{H}_{WG} , and their interaction \mathcal{H}_I [41–43]. In the paramagnetic regime, spins are considered as non-interacting, $\mathcal{H}_M \approx -g_S \mu_B \sum_j \vec{B} \cdot \vec{S}_j$, while the waveguide Hamiltonian \mathcal{H}_{WG} is formulated in terms of right-moving r_ω and left-moving l_ω photons, $\mathcal{H}_{WG} = \int_{\Omega_-}^{\Omega_+} d\omega \hbar \omega (r_\omega^\dagger r_\omega + l_\omega^\dagger l_\omega)$ with Ω_\pm representing the cut-off frequencies. The spin-photon interaction, detailed in [36], is expressed as $\mathcal{H}_I = \sum_j \int_{\Omega_-}^{\Omega_+} d\omega \vec{B}_{\text{rms},\perp}(\omega, \vec{r}_j) \cdot \vec{S}_j(r_\omega + l_\omega + \text{h.c.})$. Here, $B_{\text{rms},\perp}(\omega, \vec{r}_j)$ denotes the root-mean-square fluctuations, at frequency ω and spin position \vec{r}_j , of the waveguide magnetic field confined within the xz plane (Fig. 1a).

The spin resonances can be fitted with the following expression, derived from \mathcal{H} using input-output theory (see [11, 44–46] and [36] for details),

$$S_{21} = \left| 1 - \frac{G}{G + \Gamma + i(\Omega - \omega)} \right| \quad (1)$$

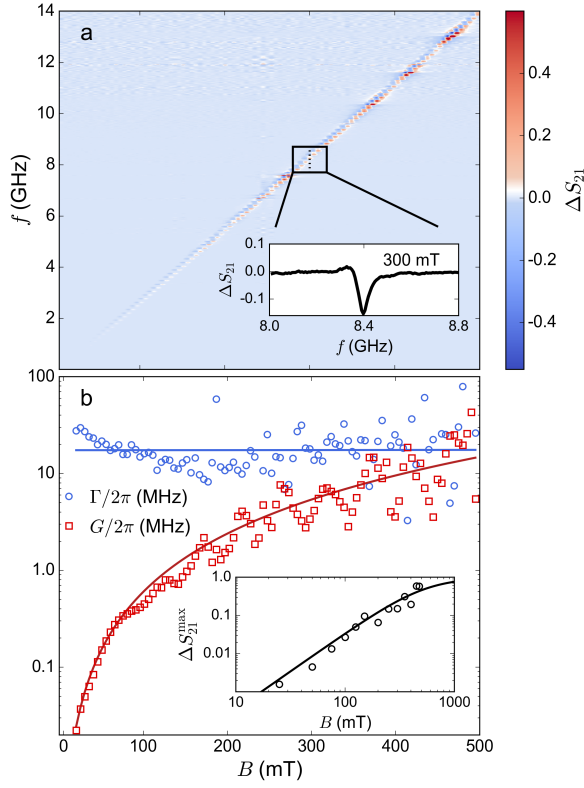


FIG. 2. (a) Two-dimensional plot of the microwave transmission, measured at $T = 2$ K, through a superconducting wave guide coupled to a DPPH polycrystalline pellet. The inset shows the Lorentzian shape of a spin resonance. (b) Collective spin-photon coupling G and decay rate Γ obtained by fitting the transmission data with Eq. (1). The lines are least-square fits based on Eq. (2), for G , and on a constant function $\Gamma/2\pi \simeq 18$ MHz. The inset shows the maximum transmission visibility as a function of magnetic field (open dots) and the prediction derived from Eq. (1).

to obtain the collective spin-photon coupling G and the decay rate Γ , which parameterizes the losses. Values extracted at $T = 2$ K are shown in Fig. 2b.

We find a nearly constant $\Gamma/2\pi \simeq 18$ MHz. This value is larger than the spin dephasing rate $\gamma_\phi/2\pi = 1/2\pi T_2 \simeq 4.8$ MHz ($T_2 = 33$ ns) obtained from time-resolved electron paramagnetic resonance experiments [36], thus showing that the resonance width has contributions from inhomogeneous broadening. The spin-photon coupling increases with B , reaching remarkably high values, very close to Γ , for $B \simeq 0.5$ T, when the resonance visibility ΔS_{21}^{\max} (inset of Fig. 2) also approaches unity. For N quasi-independent spin emitters, G is given by

$$G = 2\pi\lambda_\Omega^2 N_{\text{eff}} \quad (2)$$

where $\lambda_\Omega^2 = \alpha\Omega$ is the spin-photon coupling spectral density for a one-dimensional waveguide and N_{eff} is the effective spin number at the given temperature, proportional to the spin polarization along \vec{B} . Figure 2b shows

that Eq. (2) accounts well for the observed coupling enhancement, with $N_{\text{eff}} = N \tanh(\hbar\Omega/2k_B T)$ [47] and the constant α as the sole free parameter.

The enhancement with N_{eff} reflects the increase in the decay rate from superradiant collective states. In the single-photon limit and at zero temperature, this serves as a signature of the formation of Dicke states. In our case, these are thermal collective states that emit in a superradiant manner, $G \propto N_{\text{eff}}$, while the emission to other channels, given by Γ , is determined by the single-spin decay rates. The experimental data confirm that, at this temperature, DPPH molecules mainly act as non-interacting $S = 1/2$ emitters and that it is possible to reach a regime in which collective spin-photon couplings become dominant over the decay rates.

Lowering temperature allows exploring how AF correlations along spin chains [22, 23, 48] modify the interaction with microwave photons. Figure 3 shows transmission data measured at a fixed $B = 125$ mT as a function of ω and (decreasing) T . The spin resonance first gets enhanced on cooling below 2 K, as a result of the higher spin polarization, but then its visibility decreases (see Fig. 4a). This is accompanied by a significant broadening, by a factor ten between 1.5 K to 10 mK, and, as Fig. 3c shows, by a 7 % upwards shift of the average resonance frequency Ω .

Experiments performed for different input microwave powers [36] lead to the same results. Therefore, the broadening is not associated with any spin saturation effect. It is also much larger than the line width arising from the weak anisotropy, less than 0.1 %, between the principal g_S -factors of DPPH [21]. A possible origin is the combined effect of growing spin correlations and of a weak anisotropy in the spin-spin exchange interactions. As a result, each DPPH crystallite would acquire a different $\Omega(\psi)$, depending on its orientation ψ with respect to the \vec{B} . The ensuing inhomogeneous broadening makes DPPH molecules ‘distinguishable’ and therefore breaks down the Dicke state. This effect gives further evidence for the formation of spin chains in DPPH.

In order to provide a firmer basis to this interpretation, we model the light-matter Hamiltonian incorporating *intrinsic* interactions into the spin Hamiltonian \mathcal{H}_M . We treat the spin chains in DPPH by a mean field (MF) approximation (see [49] and [36] for details):

$$\mathcal{H}_M = -g_S\mu_B\vec{B}(\vec{M}_1 + \vec{M}_2) + \vec{M}_1\hat{J}\vec{M}_2 \quad (3)$$

where \vec{M}_1 and \vec{M}_2 are the macro-spin vectors of the two magnetic sublattices within each chain and the exchange interaction tensor $\hat{J} = \text{diag}(J, J(1 + \epsilon \sin \psi), J(1 + \epsilon \cos \psi))$ introduces an uniaxial anisotropy along \vec{e} . The exchange constant J has been determined comparing the Weiss temperature $\theta = -0.6$ K, which determines the paramagnetic susceptibility measured between 1 K and 10 K (Fig. 1b

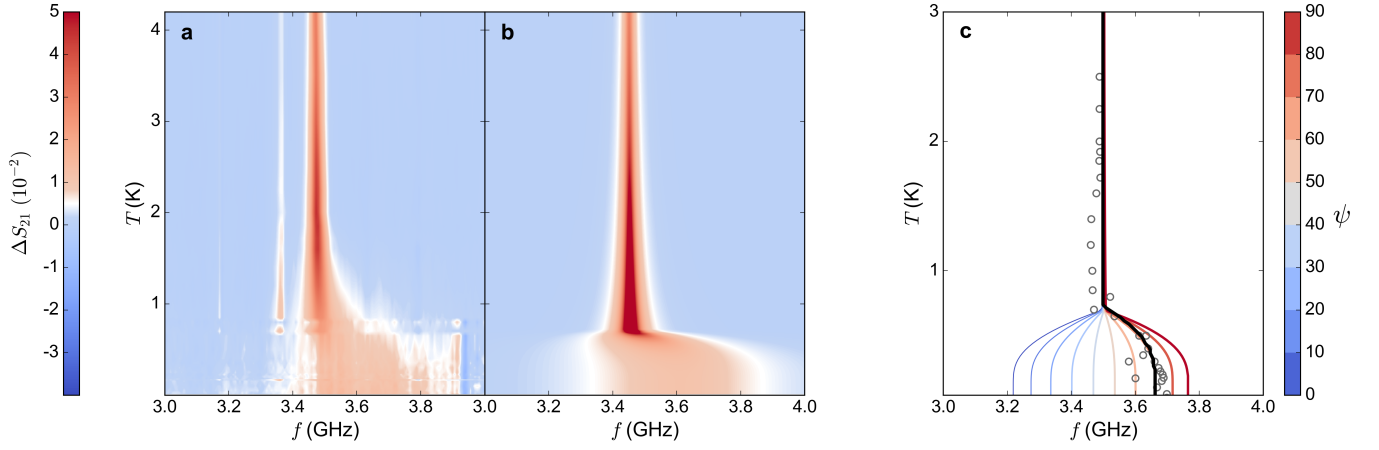


FIG. 3. Experimental (a) and simulated (b) microwave transmission at $B = 125$ mT. (c) Dependence of the spin resonance frequency Ω on the angle ψ between the magnetic field and the magnetic anisotropy axis of DPPH. The line thickness is proportional to the contribution to the spin resonance, which increases for molecules forming larger angles and therefore, for larger frequencies. The central Ω obtained from the simulations in (b) is given by the solid black line while the grey open symbols are experimental data.

and [36]), with the MF prediction $\theta = -J/k_B$. Then, Ω can be obtained, for any angle ψ between \vec{B} and \vec{e} , by solving the Landau-Lifshitz-Gilbert equation in the linear regime [50]. As expected, the results (Fig. 3c) show that the anisotropy introduces a distribution of resonance frequencies with a larger contribution from $\Omega(\psi \simeq \pi/2)$. This explains the change in the average Ω (see Fig. 3c) and the resonance broadening (see Fig. 4b) that are observed experimentally.

Again, S_{21} can be computed using input-output theory [51] (see also [36]). However, it is essential to consider two limitations of the MF theory. Firstly, MF overestimates the sharpness of changes occurring when T approaches $|\theta| \equiv T_N$, as it predicts a transition towards an AF phase that does not occur in 1D systems. Besides, the MF low-energy excitations involve tilting the relative orientations of \vec{M}_1 and \vec{M}_2 . In reality, bosonic spin-wave excitations occur. Our theory incorporates spin wave modes by assuming that, below T_N , excitations are magnons with $\Omega(\psi)$ calculated by MF. Consequently, the classical Hamiltonian (3) is replaced by the spin-wave one $\mathcal{H}_M = \hbar\Omega(\psi)(b^\dagger b + 1/2)$, where $[b, b^\dagger] = 1$. Then, S_{21} can be calculated as follows [36]:

$$S_{21} = \left| \frac{1}{1 + \int d\psi \sin \psi \frac{\lambda_\Omega^2 N_{\text{eff}}(T_N)}{-\Gamma_{\text{SW}} + i(\Omega(\psi) - \omega)}} \right| \quad (4)$$

with $\Gamma_{\text{SW}} \approx \Gamma(T_N)$. This formula gives the transmission shown in Fig. 3b, which, apart from the discussed sharpness, accounts well for the experimental results. Importantly, we take a closer look at the temperature dependence of the visibility in Fig. 4a. The red dotted curve illustrates $\Delta S_{21}^{\text{max}}$ calculated with the classical MF Hamiltonian, increasing as T decreases, while the solid

line represents (4), which includes the spin-wave character of the excitations. Only the latter agrees with the experimental data. The nearly constant $\Delta S_{21}^{\text{max}}$ observed below 600 mK therefore provides direct evidence for a change in the statistics of the elementary spin excitations that couple to the microwave photons.

In summary, we have observed a crossover from quasi identical spins collectively interacting with microwave photons to a regime governed by 1D magnetic correlations. In the former, paramagnetic region, spin-photon couplings comparable to the decay rates have been achieved, thus providing a close equivalent, for a waveguide, to the strong coupling regime that is often encountered only with cavities. When T decreases and spin-spin interactions gain prominence, a breakdown of the collective superradiant modes occurs, because different molecules are no longer equivalent to each other. Transmission data allow detecting, and estimating, the anisotropy in the spin-spin interaction along each chain. Besides, we find that its temperature dependence reflects the change in the spin excitation statistics. As Fig. 4b illustrates, when the material is paramagnetic these are single spin flips, while antiferromagnetic interactions stabilize bosonic magnon excitations. These results illustrate the delicate interplay between light-mediated and intrinsic matter interactions within a wQED scenario.

This work has received support from grants TED2021-131447B-C21 and PID2022-140923NB-C21 funded by MCIN/AEI/10.13039/501100011033, ERDF ‘A way of making Europe’ and ESF ‘Investing in your future’, from the Gobierno de Aragón grant E09-17R-Q-MAD, from the European Union Horizon 2020 research and innovation programme through FET- OPEN grant FATMOLS-No862893, and from the Spanish Ministry for Digi-

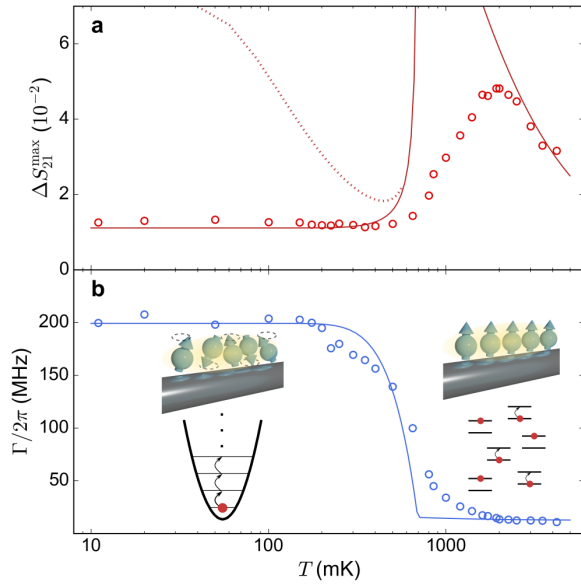


FIG. 4. (a) Maximum visibility obtained from the experimental results shown in Fig. 3a (red points) and from theoretical simulations based on describing the spin chains with either the classical mean field model (dotted red line) or the quantum magnon Hamiltonian (solid red line, extracted from Fig. 3b). (b) Experimental (open blue symbols) and theoretical (solid blue line) resonance width. The inset illustrates the nature of the spin excitations that couple to propagating photons: single spin excitations in the paramagnetic regime and bosonic spin waves in the low- T region.

tal Transformation and Civil Service and NextGenerationEU through the Quantum Spain project (Digital Spain 2026 Agenda). It also forms part of the Advanced Materials and Quantum Communication programmes with funding from European Union NextGenerationEU (PRTR-C17.I1), MCIN, Gobierno de Aragón, and CSIC (PTI001).

- [1] M. O. Scully and A. A. Svidzinsky, *Science* **325**, 1510 (2009).
- [2] M. O. Scully, *Phys. Rev. Lett.* **102**, 143601 (2009).
- [3] R. H. Dicke, *Phys. Rev.* **93**, 99 (1954).
- [4] R. G. DeVoe and R. G. Brewer, *Phys. Rev. Lett.* **76**, 2049 (1996).
- [5] S. Haroche, *Rev. Mod. Phys.* **85**, 1083 (2013).
- [6] O. Astafiev, A. M. Zagoskin, A. A. Abdumalikov, Y. A. Pashkin, T. Yamamoto, K. Inomata, Y. Nakamura, and J. S. Tsai, *Science* **327**, 840 (2010).
- [7] A. F. van Looy, A. Fedorov, K. Lalumière, B. C. Sanders, A. Blais, and A. Wallraff, *Science* **342**, 1494 (2013).
- [8] A. Javadi, I. Söllner, M. Arcari, S. L. Hansen, L. Midolo, S. Mahmoodian, G. Kiršanskė, T. Pregnolato, E. H. Lee, J. D. Song, S. Stobbe, and P. Lodahl, *Nat. Commun.* **6**, 8655 (2015).
- [9] M. O. Araújo, I. Krešić, R. Kaiser, and W. Guerin, *Phys. Rev. Lett.* **117**, 073002 (2016).
- [10] J. D. Hood, A. Goban, A. Asenjo-Garcia, M. Lu, S.-P. Yu, D. E. Chang, and H. J. Kimble, *Proc. Natl. Acad. Sci. U.S.A.* **113**, 10507 (2016).
- [11] N. V. Corzo, B. Gouraud, A. Chandra, A. Goban, A. S. Sheremet, D. V. Kupriyanov, and J. Laurat, *Phys. Rev. Lett.* **117**, 133603 (2016).
- [12] H. L. Sørensen, J.-B. Béguin, K. W. Kluge, I. Iakoupov, A. S. Sørensen, J. H. Müller, E. S. Polzik, and J. Appel, *Phys. Rev. Lett.* **117**, 133604 (2016).
- [13] P. Türschmann, N. Rotenberg, J. Renger, I. Harder, O. Lohse, T. Utikal, S. Götzinger, and V. Sandoghdar, ArXiv e-prints (2017), [arXiv:1702.05923 \[quant-ph\]](https://arxiv.org/abs/1702.05923).
- [14] P. Solano, P. Barberis-Blostein, F. K. Fatemi, L. A. Orozco, and S. L. Rolston, ArXiv e-prints (2017), [arXiv:1704.07486 \[quant-ph\]](https://arxiv.org/abs/1704.07486).
- [15] A. Goban, C.-L. Hung, J. D. Hood, S.-P. Yu, J. A. Muniz, O. Painter, and H. J. Kimble, *Phys. Rev. Lett.* **115**, 063601 (2015).
- [16] N. V. Corzo, J. Raskop, A. Chandra, A. S. Sheremet, B. Gouraud, and J. Laurat, *Nature* **566**, 359 (2019).
- [17] R. Pennetta, D. Lechner, M. Blaha, A. Rauschenbeutel, P. Schneeweiss, and J. Volz, *Phys. Rev. Lett.* **128**, 203601 (2022).
- [18] A. Glicenstein, G. Ferioli, A. Browaeys, and I. Ferrier-Barbut, *Opt. Lett.* **47**, 1541 (2022).
- [19] A. Tiranov, V. Angelopoulou, C. J. van Diepen, B. Schirnski, O. A. D. Sandberg, Y. Wang, L. Midolo, S. Scholz, A. D. Wieck, A. Ludwig, A. S. Sørensen, and P. Lodahl, *Science* **379**, 389 (2023).
- [20] A. Vylegzhanin, D. J. Brown, A. Raj, D. F. Kornovan, J. L. Everett, E. Brion, J. Robert, and S. N. Chormaic, (2023), [arXiv:2305.05186 \[physics.atom-ph\]](https://arxiv.org/abs/2305.05186).
- [21] D. Žilić, D. Pajić, M. Jurić, K. Molčanov, B. Rakvin, P. Planinić, and K. Zadro, *J. Magn. Reson.* **207**, 34 (2010).
- [22] H. Blöte, *Physica B+C* **79**, 427 (1975).
- [23] L. de Jongh and A. Miedema, *Adv. Phys.* **23**, 1 (1974).
- [24] D. MacNeill, J. T. Hou, D. R. Klein, P. Zhang, P. Jarillo-Herrero, and L. Liu, *Phys. Rev. Lett.* **123**, 047204 (2019).
- [25] C. W. Zollitsch, S. Khan, V. T. T. Nam, I. A. Verzhbitskiy, D. Sagkovits, J. O'Sullivan, O. W. Kennedy, M. Strungaru, E. J. G. Santos, J. J. L. Morton, G. Eda, and H. Kurebayashi, *Nat. Commun.* **14**, 2619 (2023).
- [26] S. D. Jenkins, J. Ruostekoski, J. Javanainen, S. Jennewein, R. Bourgain, J. Pellegrino, Y. R. P. Sortais, and A. Browaeys, *Phys. Rev. A* **94**, 023842 (2016).
- [27] L. Corman, J. L. Ville, R. Saint-Jalm, M. Aïdelsburger, T. Bienaimé, S. Nascimbène, J. Dalibard, and J. Beugnon, *Phys. Rev. A* **96**, 053629 (2017).
- [28] D. Petrosyan and K. Mølmer, *Phys. Rev. A* **103**, 023703 (2021).
- [29] J. Román-Roche, F. Luis, and D. Zueco, *Phys. Rev. Lett.* **127**, 167201 (2021).
- [30] F. J. Garcia-Vidal, C. Ciuti, and T. W. Ebbesen, *Science* **373**, eabd0336 (2021).
- [31] F. Schlawin, D. M. Kennes, and M. A. Sentef, *Appl. Phys. Rev.* **9**, 011312 (2022).
- [32] M. Mergenthaler, J. Liu, J. J. Le Roy, N. Ares, A. L. Thompson, L. Bogani, F. Luis, S. J. Blundell, T. Lancaster, A. Ardavan, G. A. D. Briggs, P. J. Leek, and E. A. Laird, *Phys. Rev. Lett.* **119**, 147701 (2017).
- [33] W. Voesch, M. Thiemann, D. Bothner, M. Dressel, and

- M. Scheffler, *Phys. Procedia* **75**, 503 (2015).
- [34] S. Lenz, D. Hunger, and J. van Slageren, *Chem. Commun.* **56**, 12837 (2020).
- [35] D. E. Williams, *J. Am. Chem. Soc.* **88**, 5665 (1966).
- [36] See Supplemental Material at [URL] for detailed descriptions of the sample characterisation and the transmission experiments, as well as for the theoretical elaborations leading to the main text equations, which includes Refs. [21, 22, 32, 35, 37, 38, 46, 47, 51–61].
- [37] H. Ohya-Nishiguchi, *Bull. Chem. Soc. Jpn.* **52**, 3480 (1979).
- [38] T. Fujito, *Bull. Chem. Soc. Jpn.* **54**, 3110 (1981).
- [39] C. Clauss, D. Bothner, D. Koelle, R. Kleiner, L. Bogani, M. Scheffler, and M. Dressel, *Appl. Phys. Lett.* **102**, 162601 (2013).
- [40] I. Gimeno, V. Rollano, D. Zueco, Y. Duan, M. C. de Ory, A. Gomez, A. Gaita-Ariño, C. Sánchez-Azqueta, T. Astner, D. Granados, S. Hill, J. Majer, E. Coronado, and F. Luis, *Phys. Rev. Appl.* **20**, 044070 (2023).
- [41] H. T. Dung, L. Knöll, and D.-G. Welsch, *Phys. Rev. A* **66**, 063810 (2002).
- [42] D. Dzsoťjan, A. S. Sørensen, and M. Fleischhauer, *Phys. Rev. B* **82**, 075427 (2010).
- [43] K. Lalumière, B. C. Sanders, A. F. van Loo, A. Fedorov, A. Wallraff, and A. Blais, *Phys. Rev. A* **88**, 043806 (2013).
- [44] S. Fan, S. E. Kocabaş, and J.-T. Shen, *Phys. Rev. A* **82**, 063821 (2010).
- [45] Y.-L. L. Fang, H. Zheng, and H. U. Baranger, *EPJ Quantum Technol.* **1**, 3 (2014).
- [46] E. Sánchez-Burillo, L. Martín-Moreno, J. J. García-Ripoll, and D. Zueco, *Phys. Rev. A* **94**, 053814 (2016).
- [47] I. Gimeno, W. Kersten, M. C. Pallarés, P. Hermosilla, M. J. Martínez-Pérez, M. D. Jenkins, A. Angerer, C. Sánchez-Azqueta, D. Zueco, J. Majer, A. Lostao, and F. Luis, *ACS Nano* **14**, 8707 (2020).
- [48] J. C. Bonner and M. E. Fisher, *Phys. Rev.* **135**, A640 (1964).
- [49] T. Nagamiya, K. Yosida, and R. Kubo, *Adv. Phys.* **4**, 1 (1955).
- [50] F. Keffer and C. Kittel, *Phys. Rev.* **85**, 329 (1952).
- [51] C. W. Gardiner and M. J. Collett, *Phys. Rev. A* **31**, 3761 (1985).
- [52] N. D. Yordanov, *Appl. Magn. Reson.* **10**, 339 (1996).
- [53] A. D. Kent, S. von Molnár, S. Gider, and D. D. Awschalom, *J. Appl. Phys.* **76**, 6656 (1994).
- [54] G. R. Stewart, *Rev. Sci. Instrum.* **54**, 1 (1983).
- [55] J. H. V. Vleck, *Phys. Rev.* **74**, 1168 (1948).
- [56] P. W. Anderson and P. R. Weiss, *Rev. Mod. Phys.* **25**, 269 (1953).
- [57] T. Hümmer, F. J. García-Vidal, L. Martín-Moreno, and D. Zueco, *Phys. Rev. B* **87**, 115419 (2013).
- [58] A. Ghirri, C. Bonizzoni, F. Troiani, N. Buccheri, L. Beverina, A. Cassinese, and M. Affronte, *Phys. Rev. A* **93**, 063855 (2016).
- [59] J. Garcia-Palacios, J. Gong, and F. Luis, *J. Phys. Condens. Matter* **21**, 456006 (2009).
- [60] S. V. Vonsovskii, *Ferromagnetic resonance* (Pergamon Press, 1966).
- [61] M. P. Ross, *Spin dynamics in an antiferromagnet*, Diploma thesis, Technische Universität München (2013).

Waveguide QED at the onset of spin-spin correlations. Supplemental Material

Sebastián Roca-Jerat,¹ Marcos Rubín-Osanz,¹ Mark D. Jenkins,¹
Agustín Camón,¹ Pablo J. Alonso,¹ David Zueco,¹ and Fernando Luis¹

¹*Instituto de Nanociencia y Materiales de Aragón (INMA),
CSIC-Universidad de Zaragoza, Zaragoza 50009, Spain*

I. SAMPLE PREPARATION AND STRUCTURAL CHARACTERIZATION

DPPH (2,2-diphenyl-1-picrylhydrazyl) is a free radical molecule hosting a spin $S = 1/2$ with a nearly isotropic $g_S = 2.004$ factor, very close to that of a free electron.^{1,2} This molecule is a widely used standard in Electron Paramagnetic Resonance (EPR).³ DPPH samples used throughout this work were purchased, in powder form, from Sigma Aldrich (reference D9132).

Even though solvent-free DPPH has been known for a long time,¹ a full structural determination was not performed until quite recently.² The results of powder X-ray diffraction experiments performed on our sample are shown in Fig. S1. They suggest that it corresponds to the DPPH-III structure,² shown in Fig. 1a in the main text, which contains two inequivalent DPPH sites, referred to as A and B sublattices.

II. MAGNETIC CHARACTERIZATION

A. Magnetic properties measurements

The dc magnetic susceptibility and magnetic isotherms were measured above 2 K in a Magnetic Properties Measurement System (MPMS) by Quantum Design, a commercial magnetometer based on a dc-SQUID, operated by the Servicio de Apoyo a la Investigación (SAI) of the University of Zaragoza. In addition, measurements were

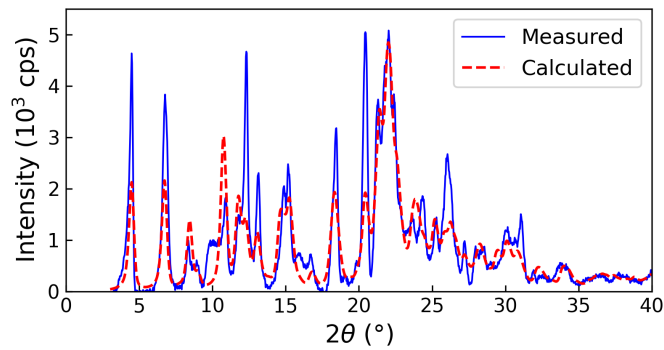


FIG. S1. **Determination of the crystal structure of the DPPH samples with X-ray diffraction experiments.** Powder diffraction experiment performed on a DPPH sample (blue solid line) and the calculated pattern for the DPPH-III crystal structure (red dashed line).²

also performed, for $0.3 \text{ K} \leq T \leq 10 \text{ K}$, with a home-made micro-Hall magnetometer⁴ mounted in the insert of a Physical Properties Measurement System (PPMS), also by Quantum Design and operated by the SAI. The magnetometer (Fig. S2) consists of two semiconducting layers of GaAs and $\text{Al}_{1-\alpha}\text{Ga}_\alpha\text{As}$, shaped in the form of a double cross, with a two-dimensional electron gas confined at the interface between the two materials. A current I_{ac} is introduced through the main arm and a magnetic field \vec{B} is applied parallel to it. The DPPH sample was placed on the edge of one of the two Hall crosses of the device and fixed/thermalized with Apiezon N grease. Its magnetization \vec{M} generates an additional magnetic field \vec{B}_M , perpendicular to the plane of the device, which induces a Hall voltage V_{Hall} proportional to $|\vec{M}|$. In order to reduce noise and detect this signal, the current was modulated at a frequency of 107 Hz, with an $I_{ac} = 10 \mu\text{A}$ amplitude, and the reference voltage V_{ref} in the bare cross was subtracted from V_{Hall} by means of a differential lock-in amplifier.

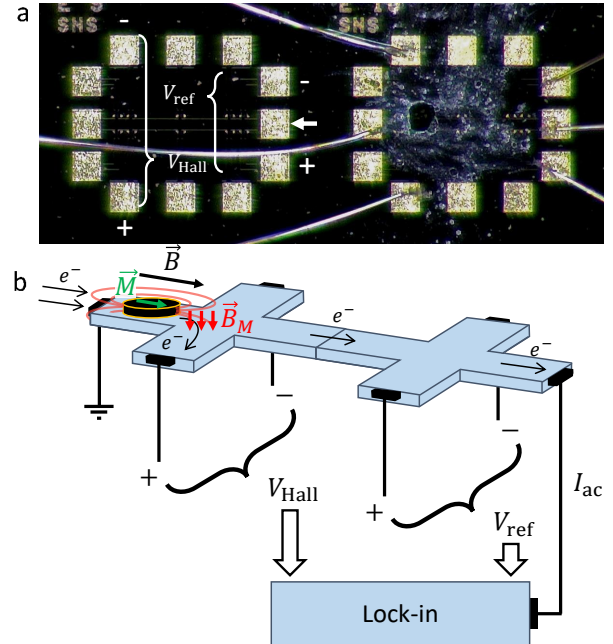


FIG. S2. **Micro-Hall magnetometry.** (a) Optical microscopy image showing a bare micro-Hall chip with two Hall crosses (left) and a chip hosting a DPPH sample on top of one of them (right). (b) Schematic image of the magnetometer, illustrating the differential detection method used to measure the Hall voltage associated with the sample's magnetization.

The dc-magnetic susceptibility χ measured between 0.35 and 100 K with a magnetic field $B = 0.1$ T can be found in Fig. 1 of the main text, as the product χT . Figure S3 shows two complementary representations of these data: χ and $1/\chi$ (Curie-Weiss plot) vs temperature. From room temperature down to about 35 K, χ follows a Curie-Weiss law $\chi = C/(T - \theta)$, with C the Curie constant and θ the Weiss temperature. We find that $C = 0.320(1)$ emu K/mol Oe measured in this region is smaller, by a factor $x \equiv C/C_{S=1/2} \cong 0.85$, than $C_{S=1/2} = N_A g_S^2 / 4k_B = 0.375$ emu K/mol Oe that would be expected for isolated $S = 1/2$ spins having the g-factor $g_S = 2.004$ reported for DPPH.² This suggests that a fraction of DPPH molecules are in their oxidized form, which is diamagnetic, i.e. has $S = 0$. The finite negative $\theta = -21$ K reflects the existence of relatively strong antiferromagnetic (AF) interactions. These interactions lead to the drop in the χT product, proportional to the effective magnetic moment squared, that is observed experimentally. A quite similar behaviour has been observed in diverse DPPH derivatives.^{2,5,6} It is associated with the coupling between nearest neighbour molecules, which tend to form AF dimers with an $S = 0$ ground state. In the DPPH-III structure, such spin dimers are formed by DPPH molecules belonging to the A crystal sublattice, see Fig. 1a in the main text and 2.

Below 10 K, χT shows a second drop. In this temperature region, χ follows also a Curie-Weiss law, but with a smaller $C \equiv C_B = 0.154(1)$ emuK/mol Oe and a much smaller $\theta = -0.6$ K. This behaviour probably reflects the weaker interactions between spins in sublattice B of DPPH-III. The response remains paramagnetic down to very low- T , with no clear indication of a phase transition. It is consistent with the formation of either AF dimers or low dimensional (1D) antiferromagnetic chains. However, specific heat data, discussed in section IIB, point to the formation of chains. We have calculated the dc susceptibility of finite chains of $N \leq 8$ $S = 1/2$ spins coupled by a Heisenberg AF coupling. Details of the model and the calculations are given in section V A below. The experimental χT can be described by the combination of two contributions: one arising from AF dimers of A-type DPPH molecules and another one resulting from AF chains formed within the B sub-lattice. The reason why the low- T χ can be accounted for with a model that considers small- N chains is that the contribution per spin to the total susceptibility tends to vanish as $N \rightarrow \infty$. The uncompensated spins in odd- N chains are responsible for the incomplete cancellation of χT as $T \rightarrow 0$. The origin of finite size chains can be associated with the presence of about 15% of diamagnetic DPPH molecules, which are randomly distributed over the crystal lattice.

Magnetic isotherms measured at 0.5, 1, 2, 5 and 10 K for magnetic fields up to 8 T are also shown in Fig. S3. Below 5 K, the theory for non-interacting paramagnetic spins (solid lines) overestimates the observed magnetization (light dots), which is partially suppressed at low fields by AF interactions.

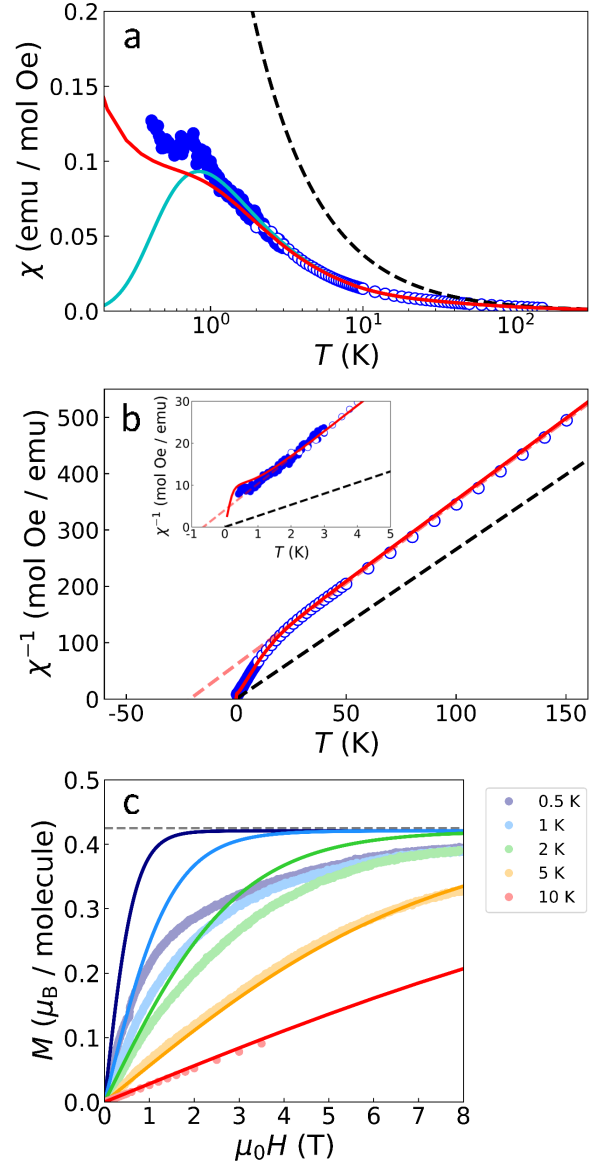


FIG. S3. **Magnetic characterization.** (a) dc-magnetic susceptibility χ of a DPPH powdered sample measured between 0.35 and 300 K with a magnetic field of 0.1 T. Open dots were measured with a dc-SQUID magnetometer, solid dots with a micro-Hall magnetometer. The predictions of a model of infinite AF chains (red solid line) and a model of AF dimers (cyan solid line) are compared to the experimental data. The black dashed line is the Curie law for a fully paramagnetic DPPH sample. (b) Curie-Weiss plot of the reciprocal susceptibility χ^{-1} vs temperature. The light red dashed line is a least square linear fit of data measured above 50 K. It gives a Weiss temperature $\theta = -21$ K associated with the formation of AF dimers in sublattice A. Inset: close up plot of the low temperature region data, which follow a Curie-Weiss law (light red dashed line) with $\theta = -0.65$ K associated to the formation of AF chains in sublattice B. (c) Magnetic isotherms, measured at 0.5, 1, 2, 5 and 10 K for magnetic fields up to 8 T. The lines show the dependence expected for non-interacting paramagnetic spins.

B. Heat capacity measurements

Heat capacity experiments were carried out also in a PPMS. The calorimeter consists of a sapphire disc — the sample holder — on which the sample is placed. This holder integrates a heater and thermometer, and it is connected to a thermal reservoir by thin gold wires. Sample and holder are put in mutual thermal contact with apiezon N grease. Measurements are performed with controlled pressure conditions in the sample chamber of the PPMS, that is, constant-pressure heat capacity is measured. The heat capacity of the sample is measured using a relaxation technique.⁷ A heat power is applied for a short time, increasing the temperature of both the holder and the sample. Part of the heat is transferred through the wires to the thermal reservoir. The time constant of the exponential increase and decrease of temperature during this process is proportional to the heat capacity of the combined sample plus holder system. The different holders are regularly calibrated without sample, so that the heat capacity of the holder can be subtracted from the measurement.

The zero-field specific heat of DPPH is shown in Fig. 1c of the main text. Above 2 K, it is dominated by a large contribution arising from lattice and molecular vibrations. At lower temperatures, an additional contribution shows up, which depends on magnetic field, as shown in Fig. S4. Therefore, it reflects spin excitations. The broad shape of this anomaly confirms that no phase

transition to long-range magnetic order takes place in this temperature region.

The zero-field data agree well with predictions for the specific heat of infinite AF chains,⁸ and seem to rule out the formation of dimers within the B sublattice. Lacking an analytical model for the $B \neq 0$ specific heat of infinitely long AF spin chains, we had to content ourselves with computing the heat capacity of finite chains of up to eight $S = 1/2$ spins. The model is discussed in section V A. This simplified model accounts reasonably well for data measured at low ($B \leq 0.5$ T) and high ($B > 2$ T) magnetic fields. In the latter case, it tends towards the predictions for non-interacting spins, as expected. Deviations are observed at intermediate fields (1–2 T).

III. ELECTRON PARAMAGNETIC RESONANCE EXPERIMENTS

Electron Paramagnetic Resonance (EPR) experiments were performed in a commercial Elexsys E-580 by Bruker operating in the X-band (~ 9.8 GHz). The spectrometer consists of a resonant cavity, in which the paramagnetic sample is placed, located at the center of an electromagnet. The external DC magnetic field generated by the magnet tunes the spin transition to the cavity frequency, which results in a resonant absorption of microwave power by the sample.

In continuous wave EPR (cw-EPR) experiments, the cavity is continuously irradiated while the DC magnetic field is swept slowly. The absorption signal is obtained with a field-modulation detection, in which a set of small coils apply a radio-frequency (RF) magnetic field modulation that results in a derivative-like line shape for each absorption signal. The single narrow line shape measured with this technique, shown in Fig. S5a, agrees with a spin $S = 1/2$ and $g_S = 2.004$. The line intensity I shows a paramagnetic behaviour, with IT , also shown in Fig. S5, behaving very much as χT . The line shape suggests that the line width is dominated by the homogeneous broadening down to 4 K. It is known that, in the paramagnetic phase of DPPH, exchange interactions tend to suppress the inhomogeneous broadening associated with dipole-dipole interactions⁹ via the exchange narrowing mechanism.¹⁰ This property makes DPPH a good reference material for calibrating commercial EPR systems.³

Time-domain, or pulsed, EPR experiments measure the signal emitted by the spin system after sending a series of microwave pulses to the cavity. This gives information on the relaxation and coherence of the spin system, as the detected signal depends on the dynamics of the spin state prepared by the pulses. The simplest pulsed EPR experiment is the measurement of the Free Induction Decay (FID), which is the signal that the spin system induces in the cavity after a microwave pulse generates a coherence between the two spin states of a given transition. If the spin system exhibits inhomogeneous

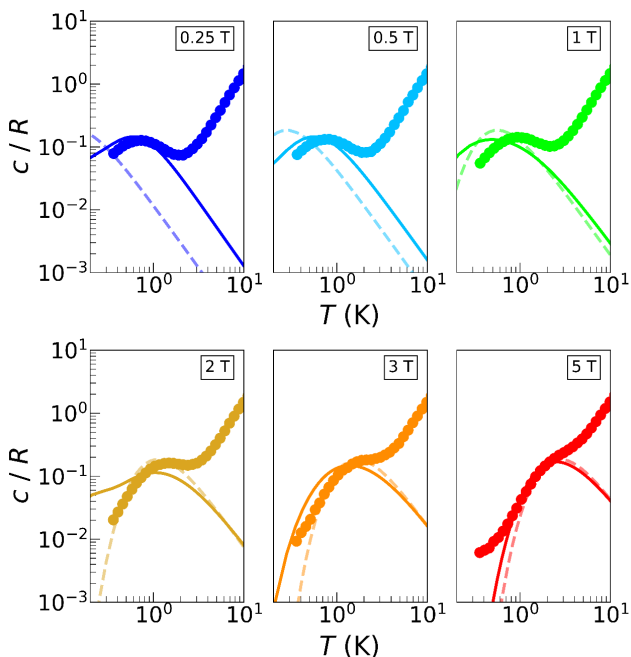


FIG. S4. Heat capacity of polycrystalline DPPH for different magnetic fields. The experimental results (dots) are compared with a theory of small AF chains (solid lines) and with the paramagnetic theory for non-interacting $S = 1/2$ spins (light dashed lines).

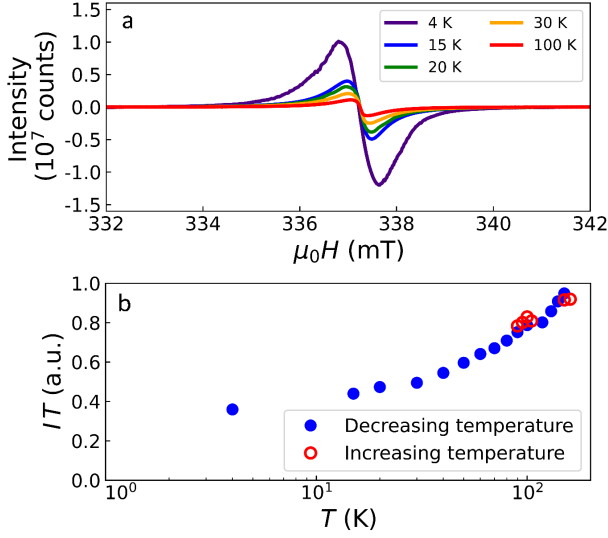


FIG. S5. **cw-EPR experiments.** (a) cw-EPR spectra of a powder DPPH sample measured at five different temperatures. (b) Evolution of the product of the intensity of the cw-EPR spectrum times temperature, measured first for decreasing temperatures (blue closed dots) and then for increasing temperatures (red open dots).

broadening, a revival of the FID signal — the ‘echo’ — can be recovered with refocusing pulses. When homogeneous broadening is dominant, there is no spin echo signal, and the phase memory time T_m of the spin system is obtained as the characteristic time constant of the FID. Time-domain EPR measurements of the FID of DPPH powder samples were carried out at 7.7 K and at room temperature. The results are shown in Fig. S6. The fit of the two signals is compatible with a homogeneous broadening $\gamma_\phi/2\pi = 1/2\pi T_m = 4.8$ MHz and 4.3 MHz at 7.7 K and room temperature, respectively. These values correspond to $T_m = 33$ ns and 37 ns, respectively. Figure S6c shows that these values are also compatible with those obtained from microwave transmission experiments at lower temperatures.

IV. ON-CHIP MICROWAVE TRANSMISSION EXPERIMENTS

A. Experimental setup

Microwave transmission experiments were performed with on-chip superconducting coplanar waveguides fabricated by optical lithography on a 100 nm Nb thin film deposited onto crystalline sapphire wafers. A 1 mm wide DPPH pellet was fixed on the 400 μm wide central line by means of apiezon N grease, see Fig. S7a. Figures S7b-c show how the superconducting chip is integrated in the ^3He - ^4He dilution refrigerator that gives access to temperatures as low as 7 mK. A cold finger (Fig. S7b) places the chip at the center of a 1 T axial superconducting mag-

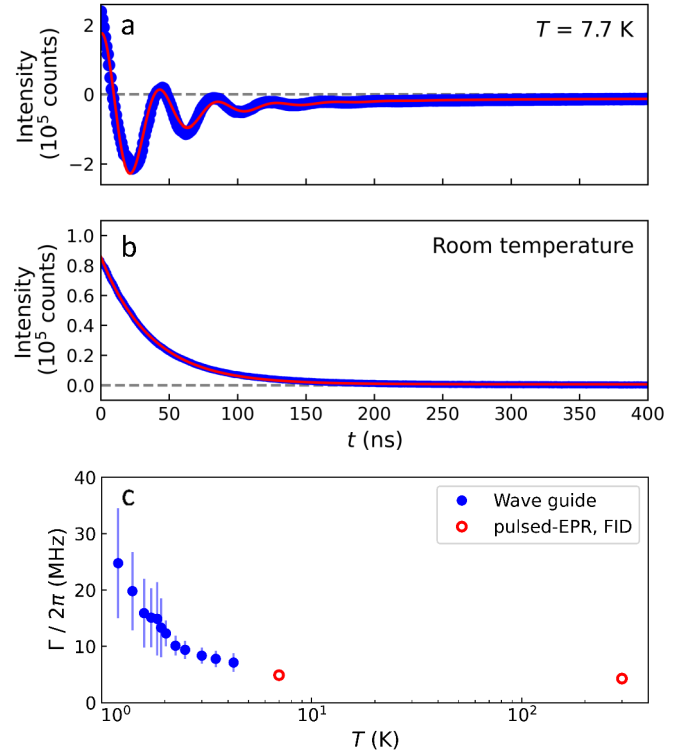


FIG. S6. **Pulsed-EPR experiments.** (a) Free Induction Decay (FID) of a DPPH powered sample measured at 7.7 K. (b) FID of the same sample measured at room temperature. (c) Temperature dependence of the DPPH absorption spectrum width. The values extracted from FID data (red open dots) are compared to those derived from on-chip microwave transmission experiments (blue closed dots).

net (Fig. S7c). The magnetic field is applied along the \hat{y} axis of the laboratory reference frame, which is parallel to the wave guide. The device is thermalized to the mixing chamber of the dilution refrigerator (Fig. S7d). The transmission S_{21} through the device was measured in the frequency range $10 \text{ MHz} \leq \omega/2\pi \leq 14 \text{ GHz}$ with a vector network analyzer. The input signal was attenuated by 50 dB before reaching the chip, while the transmitted signal was amplified by 30 dB at 4 K with a low-noise cryogenic amplifier.

B. Normalization of microwave transmission data

In the actual transmission data the microwave absorption by the DPPH spins is often masked by spurious modes, see Fig. S8a, that arise from unavoidable imperfections in the microwave circuit. The measured transmission can then be understood as the convolution:

$$S_{21} \simeq S_{21, \text{WG+DPPH}} S_{21, \text{modes}}, \quad (1)$$

of the transmission features $S_{21, \text{WG+DPPH}}$ arising from the presence of the DPPH sample on top of the waveguide with the contribution $S_{21, \text{modes}}$ arising from those modes.

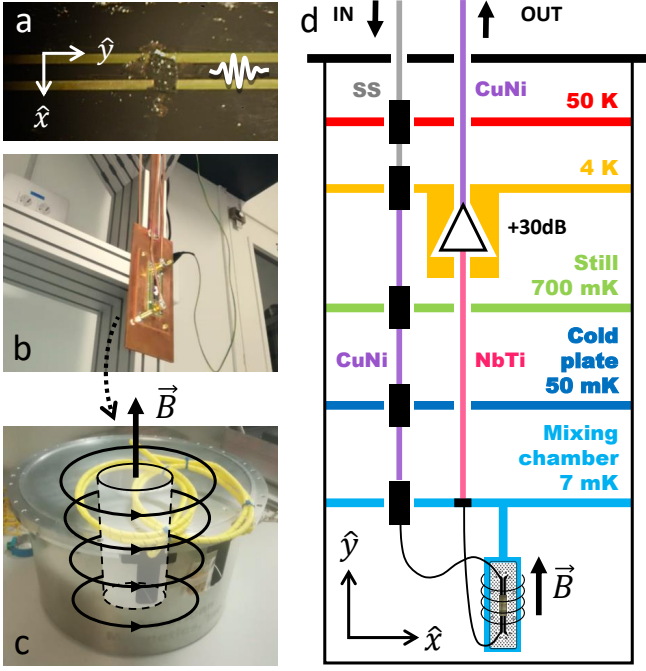


FIG. S7. **Experimental setup for on-chip transmission experiments.** (a) Microscopy image of a DPPH powder sample on top of the waveguide. (b) Cold finger hosting the superconducting chip. (c) Superconducting magnet in which the cold finger is inserted, generating a magnetic field parallel to the waveguide. (d) Scheme of the ^3He - ^4He dilution refrigerator with a base temperature $\simeq 7$ mK.

In order to obtain $S_{21, \text{WG+DPPH}}$, the raw S_{21} needs to be normalized. A simple normalization procedure exploits the magnetic field dependence of $S_{21, \text{WG+DPPH}}$:

$$S_{21, \text{WG+DPPH}}(B) \simeq 1 + \Delta S_{21}(B), \quad (2)$$

with:

$$\Delta S_{21}(B) = \frac{S_{21}(B) - S_{21}(B + \Delta B)}{S_{21}(B_{\text{ref}})}. \quad (3)$$

Here, the raw data $S_{21}(B)$ measured at a field B are normalized by subtracting from it the raw data $S_{21}(B + \Delta B)$ measured at a close field $B + \Delta B$ and dividing the result by a reference transmission measured at a fixed field B_{res} (usually $B_{\text{res}} = 0$ is chosen, or any magnetic field at which the microwave transmission shows no features associated to any spin resonances in the relevant frequency region). As shown in Fig. S8b, this method effectively removes $S_{21, \text{modes}}$ from the transmission data, provided that $S_{21, \text{modes}}$ is independent of magnetic field or that it varies sufficiently slowly with it. The normalization step ΔB is chosen to be as small as possible while avoiding the overlap of the spin resonances in $S_{21}(B)$ and $S_{21}(B + \Delta B)$. This requires that $|\Delta B| \gg \hbar\Gamma/\mu_B g_S$.

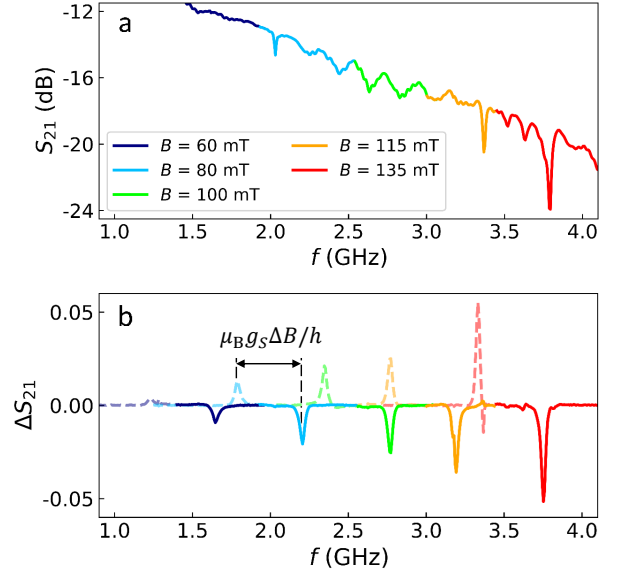


FIG. S8. **Normalization of transmission data.** (a) Raw microwave transmission data S_{21} measured on a waveguide coupled to a powdered DPPH sample at five magnetic field values. They are chosen in such a way that spin resonances at $\Omega = \mu_B g_S B / \hbar$ do not overlap. Some of these resonances are masked by spurious modes in $S_{21, \text{modes}}$. (b) Normalization of the transmission data with Eq. (3) at the same magnetic fields. Only the part of $S_{21, \text{WG+DPPH}}(B) \simeq 1 + \Delta S_{21}(B)$ that is close to Ω (solid lines) is used to extract the spin-photon coupling G and the dissipation rate Γ . The rest (dashed lines), which includes an upwards peak associated with the subtraction of $S_{21}(B + \Delta B)$ (in this example, $\Delta B < 0$), is discarded. This peak is not relevant as long as it does not overlap with the absorption peak at Ω , which sets the condition $\mu_B g_S |\Delta B| / \hbar \gg \Gamma / 2\pi$.

C. Transmission properties in the paramagnetic phase of DPPH

Figure S9 shows the field and temperature dependence of G and Γ in the paramagnetic phase of the B-type DPPH sublattice ($T > 0.7$ K). The coupling G is proportional the input frequency in a one-dimensional wave guide. Close to the spin resonance, this input frequency is approximately the spin resonance frequency $\Omega = \mu_B g_S B / \hbar$, and G can be written as (see Eq. (3) in the main text):

$$G = 2\pi\alpha\Omega N \tanh\left(\frac{\hbar\Omega}{2k_B T}\right), \quad (4)$$

where N is the total number of spins coupled to the microwave magnetic field generated by the waveguide, and α is a temperature-independent and field-independent dimensionless scaling factor. The only free parameter in the fit of G for all temperatures and magnetic fields within the paramagnetic phase is $2\pi\alpha N = 0.00441(6)$. The coupling enhancement by $N_{\text{eff}} = N \tanh(\hbar\Omega/2k_B T)$ signifies the increase in the radiative rate decay in super-radiant collective states.

For $T > 1$ K, the dissipation rate Γ is found to depend weakly on both magnetic field and temperature. The values derived from these experiments are compatible with those obtained with a conventional EPR spectrometer, see Fig. S6c. Besides, $\Gamma/2\pi \cong 8$ MHz measured at $T = 4.2$ K is also compatible with that obtained for DPPH samples coupled to coplanar resonators at the same temperature.¹¹ Remarkably, G becomes comparable to Γ for magnetic fields $B > 400$ mT. This yields a signal visibility $\max(|\Delta S_{21}|) = G/(G + \Gamma)$ close to unity. Therefore, the spin ensemble and the waveguide enter then a regime that resembles the strong coupling limit ($G \geq \Gamma$) that is commonly reached only by coupling spins to a resonator. In order to better understand how large this G actually is, it is worth estimating what it would lead to in the case of a resonator. Input-output theory¹² provides a relation between G and the coupling G_{res} to a cavity resonating at a given frequency ω

$$G_{\text{res}} = \sqrt{\frac{G\omega}{\pi}} \quad (5)$$

Using this relation, the maximum coupling $G/2\pi \simeq 12$ MHz to the line that we measure at $B = 500$ mT and $\omega/2\pi = 14$ GHz would correspond to $G_{\text{res}} \sim 0.58$ GHz. This estimate compares favourably to those reported previously for DPPH samples at coplanar superconducting resonators.^{13,14}

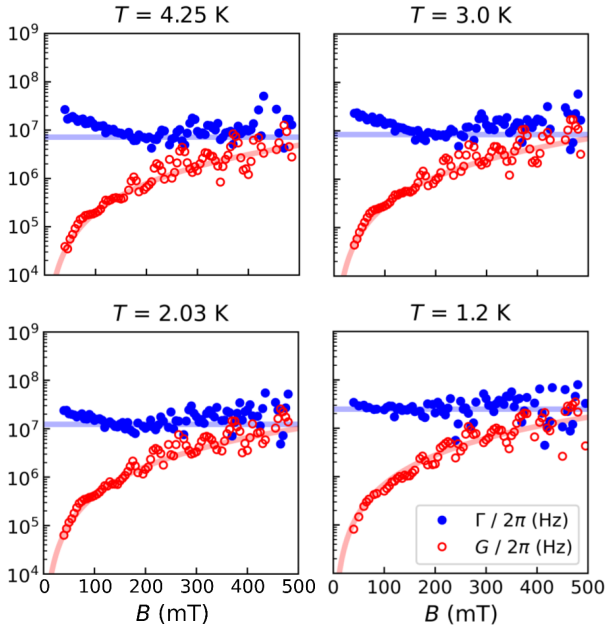


FIG. S9. **Magnetic field dependence of G and Γ at four selected temperatures within the paramagnetic phase of DPPH.** G (red open dots) and Γ (blue closed dots) values were obtained by fitting the normalized transmission data using Eq. (2) in the main text. Light solid lines show the average Γ (discarding the low magnetic field region) and the result of a least-squares fit of G with Eq. (4).

D. Effect of input microwave power

The resonance of the DPPH ensemble was measured at $T = 0.3$ K and $B = 0.22$ T with different input microwave powers P_{in} between -25 and -10 dBm. No saturation effect was observed in the resonance due to the change in P_{in} , as shown in Fig. S10.

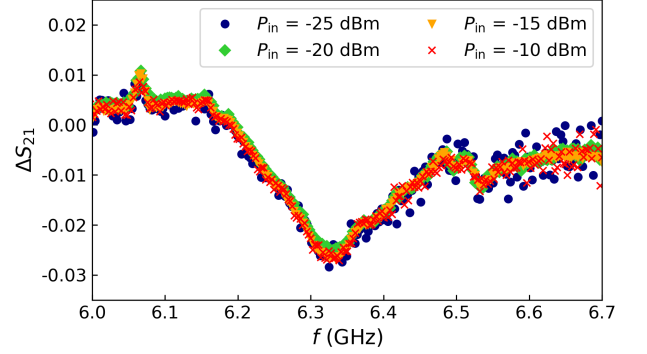


FIG. S10. **Spin resonance versus microwave power.** Normalized transmission of a waveguide coupled to a powdered DPPH sample measured at $T = 0.3$ K and $B = 0.22$ T.

V. THEORY OF ANTIFERROMAGNETIC SPIN CHAINS

A. Exact diagonalization calculation of the magnetic and thermal responses of small AF spin chains

The 1D antiferromagnetic chains that form in the B-sublattice can be described by ($\hbar = 1$):

$$\mathcal{H}_m = \sum_{i,j} \vec{S}_i \cdot \vec{J} \cdot \vec{S}_j - g\mu_B B \sum_i S_i^y. \quad (6)$$

Here, $\vec{S}_j = (\sigma_j^x, \sigma_j^y, \sigma_j^z)$ are the Pauli matrices. The anisotropy of the spin-spin interactions is encoded in the coupling tensor \vec{J} :

$$\vec{J} = \text{diag}(J, J(1 + \epsilon \sin \psi), J(1 + \epsilon \cos \psi)). \quad (7)$$

Here, ψ is the angle that the anisotropy axis $\vec{\epsilon}$ forms with z . Moreover, w.l.o.g we assume this axis lies in the yz -plane, see figure S11. The last term in \mathcal{H}_m is the Zeeman coupling to the externally applied DC magnetic field B_0 . We define the y -axis as the orientation of this field, matching the laboratory frame defined in Fig. 1a in the main text.

Using exact diagonalization we can obtain all the eigenstates of the system up to sizes not much larger than 10 spins. With them, we can calculate observables such as the specific heat or the magnetic susceptibility. Starting with the specific heat, c , we calculate it from the eigenvalues of the Hamiltonian given in Eq. (6) at a certain

temperature, T , with the following expression

$$c = \beta \left[\frac{Z''}{Z} - \left(\frac{Z'}{Z} \right)^2 \right], \quad (8)$$

where $\beta = 1/T$, $(\cdot)' = \partial_\beta$ and $Z = \text{Tr}(e^{-\beta\mathcal{H}})$.¹⁵ The terms explicitly read $Z = \sum_m e^{-\beta\epsilon_m}$, $Z' = -\sum_m e^{-\beta\epsilon_m} \epsilon_m$ and $Z'' = \sum_m e^{-\beta\epsilon_m} \epsilon_m^2$, with ϵ_m being the eigenstates of Eq. (6). We compute these energy fluctuations for the different angles ψ and sizes up to $N = 8$ spins and then we take the average. The results of the simulations are presented in Figs. S4 and 1c (main text). We confine our analysis to small-sized lattices, as the complete spectrum is necessary to compute the specific heat at finite temperatures, as discussed in Fig. S12. This limits the quantitative approach to actual experimental values.

On the other hand, for the magnetic susceptibility, we can treat perturbatively the partition function Z . In general, for a system described by some hamiltonian

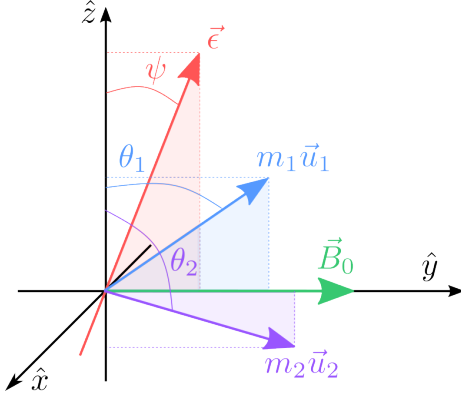


FIG. S11. Orientations of the magnetic field and of the magnetic anisotropy axis, and angle convention used in the exact diagonalization of the Hamiltonian of small 1D AF chains.

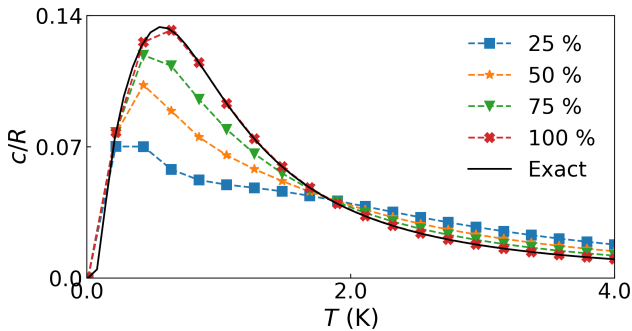


FIG. S12. Specific heat obtained through exact diagonalization. The results shown are for a 7-spin chain, as a function of temperature fixing the external magnetic field at 0.5 T. As can be seen, we only recover the analytical curve (black curve in both plots) when the totality of the system's eigenstates is considered.

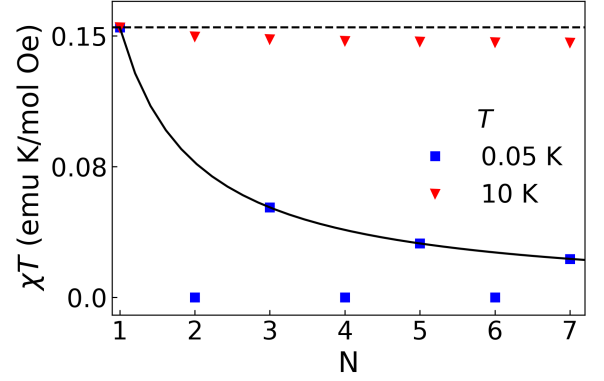


FIG. S13. Dependence of the magnetic susceptibility on the spin chain size. We show the χT product calculated, at $B = 0$, as a function of the number of spins in the chain in two regimes: low temperature (blue squares) and high temperature (red triangles). In the low-temperature regime only odd number spin chains contribute. This response (normalized by the spin number) decays with increasing chain length.

\mathcal{H}_0 that is under a perturbation Q with intensity f , i.e. $\mathcal{H} = \mathcal{H}_0 - fQ$, the susceptibility, χ , is defined as

$$\chi = \beta \left[\frac{Z_2}{Z_0} - \left(\frac{Z_1}{Z_0} \right)^2 \right], \quad (9)$$

where $Z \simeq Z_0 + \xi Z_1 + \xi^2 Z_2$ and $\xi = \beta f$.¹⁵ In our case, $Z_0 = \sum_m e^{-\beta\epsilon_m}$, $Z_1 = \sum_m e^{-\beta\epsilon_m} Q_{mm}$, and $Z_2 = \sum_{mn} e^{-\beta\epsilon_{mn}} |Q_{mn}|^2 K_{mn}$, with $Q = \frac{1}{|\vec{B}|} \vec{B} \vec{S}$, $K_{mn} = K[\beta(\epsilon_m - \epsilon_n)]$ and $K(X) = (e^X - 1)/X$.

In this case, we observe that small chains accurately reproduce the experimental curve (see Fig. S3). This phenomenon can be attributed to the fact that, with increasing chain length, the per-spin contribution to the total susceptibility diminishes. As demonstrated in Fig. S13, the susceptibility scales as $1/N$, in relation to the susceptibility of a single spin, which predominantly influences the behavior in the limit $T \rightarrow 0$. Furthermore, only chains with an odd number of spins contribute, due to their $S = 1/2$ ground state. At sufficiently high temperatures, however, chains of all lengths contribute equally, enabling the recovery of the experimental results using solely small chains, as shown in Fig. 1b in the main text.

Comparing the specific heat and the magnetic susceptibility obtained from the exact diagonalization of our model of small chains with the experimental results we found that the anisotropy in the spin-spin interactions is very small and not relevant in these experiments. This is not the case in microwave transmission experiments, where the small anisotropy plays a crucial role and significantly changes the spin resonance features, as it is shown in the main text and in section VI below.

B. Mean field theory of antiferromagnetic spin chains

For computing the transmission at very low temperatures, it is necessary to consider large chains that are beyond the scope of exact diagonalization. Therefore, we employ a mean field theory, which not only explains the underlying physics but also accounts for the experimental data both qualitatively and quantitatively, as detailed in the main text. Here, we aim to describe our application of this mean field (MF) theory to DPPH. Additionally, within the MF theory, we can compute the linear response, enabling us to characterize the transmission experiments.

We use the Bogolyubov inequality, which serves as a method for approximating the equilibrium partition function of an interacting system. This inequality arises from convexity and requires the Hamiltonian to be divided into a part that is solvable and the remaining part.

$$\mathcal{H} = \mathcal{H}_0 + \mathcal{H}_1 \implies \frac{Z}{Z_0} \geq e^{-\beta \langle \mathcal{H}_1 \rangle_0}, \quad (10)$$

with $Z = \text{Tr}[e^{-\beta \mathcal{H}}]$ the actual partition function, $Z_0 = \text{Tr}[e^{-\beta \mathcal{H}_0}]$ and $\langle \dots \rangle_0 = \text{Tr}[\dots e^{-\beta \mathcal{H}_0}] / Z_0$. Taking the logarithm in Eq. (10), an upper bound for the free energy is found:

$$F \leq F_0 + \langle \mathcal{H}_1 \rangle_0. \quad (11)$$

In antiferromagnetic systems, spins are divided in two sub-lattices, namely 1 and 2. In each sub-lattice the spin averages are the same. Therefore, we choose for \mathcal{H}_0 :

$$\mathcal{H}_0 = -\vec{\lambda}_1 \vec{M}_1 - \vec{\lambda}_2 \vec{M}_2, \quad (12)$$

where $\vec{\lambda}_\alpha$ are variational parameters that minimize the left hand side of Eq. (11) and we have used the following compact notation for the magnetization vectors:

$$\vec{M}_1 = M_1 \vec{u}_1, \quad (13)$$

$$\vec{M}_2 = M_2 \vec{u}_2. \quad (14)$$

It turns out that Z_0 only depends on the modulus $|\vec{\lambda}_\alpha|$. Thus, we can set $\lambda_\alpha \geq 0$. Considering nearest neighbor interactions, together with the angle convention used in Fig. S11, we obtain for the average:

$$\begin{aligned} \langle \mathcal{H}_1 \rangle_0 &= \lambda_1 M_1 + \lambda_2 M_2 \\ &\quad - g\mu_B B (M_1 \sin \theta_1 + M_2 \sin \theta_2) \\ &\quad + M_1 M_2 \vec{u}_1 \cdot \vec{J} \cdot \vec{u}_2, \end{aligned} \quad (15)$$

where \vec{J} is given in Eq. (7). We assume that the magnetization vectors lie also in the zy -plane, the plane spanned by the anisotropy and magnetic field vectors as depicted in Fig. S11. Simulations performed considering a generic three-dimensional orientation for the magnetisation vectors gave the same results as in the 2D case. This is easy to see since the directions of interest

are always going to be the anisotropy axis (when there is no field) or the field axis (when the field is very strong).

Inserting Eq. (15) in Eq. (11) and minimizing over the variables $\{\lambda_1, \theta_1, \lambda_2, \theta_2\}$, we end with the consistency relations:

$$\frac{\partial \langle \mathcal{H} \rangle_0}{\partial \theta_1} = 0, \quad (16a)$$

$$\lambda_1 = g\mu_B B \sin \theta_1 - M_2 \vec{u}_1 \cdot \vec{J} \cdot \vec{u}_2, \quad (16b)$$

$$M_1 = \tanh(\beta \lambda_1), \quad (16c)$$

and similar equations for sublattice 2.

In general, these equations are solved numerically. However, analytical progress can be made using symmetry arguments. We assume $\lambda_1 = \lambda_2 = \lambda$ and $M_1 = M_2 = M$. With our convention for angles (Fig. S11, we find that in either the paramagnetic phase or the spin-flop transition (see below), $\theta_1 + \theta_2 = \pi$. This condition is also applicable, in principle, to the antiferromagnetic scenario. By imposing these conditions, we derive the following expression:

$$\sin \theta_2^{\text{eq}} = \frac{g\mu_B B}{MJ[2 + \epsilon(\sin \psi + \cos \psi)]}, \quad (17)$$

with:

$$\begin{aligned} M = \tanh \left[\beta (g\mu_B B + JM \cos 2\theta_2^{\text{eq}} \right. \\ \left. - JM\epsilon(\sin^2 \theta_2^{\text{eq}} \sin \psi - \cos^2 \theta_2^{\text{eq}} \cos \psi) \right). \end{aligned} \quad (18)$$

Equations (17) and (18) are used for determining the phase diagram, as illustrated in Fig. S14. Here, we depict the numerical solutions for the equilibrium angles, $\Delta\theta_{\text{eq}}$, yielding the distinct phases. A zero value of $\Delta\theta_{\text{eq}}$ indicates that temperature and/or magnetic field are sufficient to align the magnetization vectors. A non-zero $\Delta\theta_{\text{eq}}$ signals the emergence of magnetic correlations, revealing two distinct phases: the spin-flop phase for $0 < \Delta\theta_{\text{eq}} < \pi$, and the antiferromagnetic phase for antiparallel spins. Panel (a) of Fig. S14 displays the case with perpendicular anisotropy to the magnetic field, while panel (b) considers parallel orientation. Specifically, when $\vec{B} \perp \vec{\epsilon}$ and $\psi < \pi/4$, a magnetic field weaker than $J\sqrt{2\epsilon(\sin \psi - \cos \psi)}$ results in antiparallel magnetization vectors orthogonal to the anisotropy axis, where $\theta_1 + \theta_2 = 2\pi$. This condition persists until the magnetic field B is strong enough to rotate both vectors towards the paramagnetic phase. This process is elaborated in subplots (a.1) and (b.1) of Fig. S14. The critical field at $T = 0$ is derived from Eq. (17) as $g\mu_B B^c = J(2 + \epsilon(\sin \psi + \cos \psi))$, while the Néel temperature is fixed at $T_N = J/k_B$.

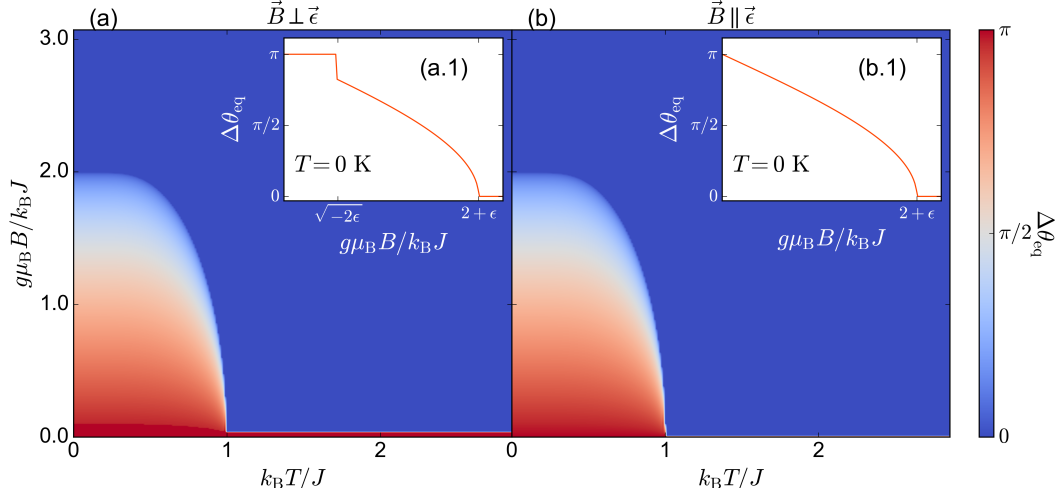


FIG. S14. **Equilibrium magnetization angles.** Phase diagram for $\Delta\theta_{\text{eq}}$ as a function of temperature and magnetic field. In (a) the anisotropy is perpendicular to the magnetic field while in (b) they are parallel. In subplots (a.1) and (b.1) we see the different behaviour at $T = 0$ that the anisotropy shows up. Since $J(1 + \epsilon) < J$, the magnetization vectors lie perpendicular to the anisotropy axis to minimize the energy. When $\psi < \pi/4$, there is a magnetic field threshold for which, below that point, magnetization remains in the perpendicular axis to $\vec{\epsilon}$. When the field is strong enough, both vectors flip to start coming parallel between them symmetrically until the paramagnetic phase is reached. This point is found to be $g\mu_B B = J\sqrt{2\epsilon(\sin\psi - \cos\psi)}$. The parameters used were $J/k_B = 0.7$ K and $J\epsilon/k_B = -0.065$ K for panels (a) and (b). In (a.1) and (b.1) an arbitrarily bigger ϵ was used for better visualization.

C. Spin dynamics: computing the resonance frequency of the chains

Mean field treatment is consistent with using the Landau-Lifshitz-Gilbert (LLG) equation for the dynamics. The LLG equation reads

$$\frac{d\vec{M}_\alpha}{dt} = -g\mu_B \vec{M}_\alpha \times \vec{B}_{\text{mol},\alpha} - \gamma \vec{M}_\alpha \times (\vec{M}_\alpha \times \vec{B}_{\text{mol},\alpha}) \quad (19)$$

with $\alpha = 1, 2$. The molecular field is given by^{16,17}

$$\vec{B}_{\text{mol},\alpha} = -\frac{1}{g\mu_B} \vec{\nabla} F, \quad (20)$$

with F the free energy computed by means of the MF, Cf. Eq. (11).

As the LLG preserves $|\vec{M}_\alpha|$, it is convenient to work in spherical coordinates, which transform Eq. (19) into the following:

$$\begin{aligned} \sin\theta_\alpha \dot{\theta}_\alpha &= -\frac{1}{M_\alpha} F_{\varphi_\alpha} - \gamma \sin\theta_\alpha F_{\theta_\alpha}; \\ \sin\theta_\alpha \dot{\varphi}_\alpha &= \frac{1}{M_\alpha} F_{\theta_\alpha} - \gamma \frac{1}{\sin\theta_\alpha} F_{\varphi_\alpha}. \end{aligned} \quad (21)$$

We have introduced the notation $F_{\theta_\alpha} \equiv \partial_{\theta_\alpha} F$. At equilibrium, the derivatives of the free energy are zero. Therefore, in the linear response regime, we perform a Taylor expansion of these derivatives, resulting in the set of linear equations:

$$\begin{pmatrix} \sin\theta_1 \dot{\theta}_1 \\ \sin\theta_1 \dot{\varphi}_1 \\ \sin\theta_2 \dot{\theta}_2 \\ \sin\theta_2 \dot{\varphi}_2 \end{pmatrix} = \begin{pmatrix} -\frac{F_{\varphi_1,\theta_1}}{M_1} & -\frac{F_{\varphi_1,\varphi_1}}{M_1} & -\frac{F_{\varphi_1,\theta_2}}{M_1} & -\frac{F_{\varphi_1,\varphi_2}}{M_1} \\ \frac{F_{\theta_1,\theta_1}}{M_1} & \frac{F_{\theta_1,\varphi_1}}{M_1} & \frac{F_{\theta_1,\theta_2}}{M_1} & \frac{F_{\theta_1,\varphi_2}}{M_1} \\ -\frac{F_{\varphi_2,\theta_1}}{M_2} & -\frac{F_{\varphi_2,\varphi_1}}{M_2} & -\frac{F_{\varphi_2,\theta_2}}{M_2} & -\frac{F_{\varphi_2,\varphi_2}}{M_2} \\ \frac{F_{\theta_2,\theta_1}}{M_2} & \frac{F_{\theta_2,\varphi_1}}{M_2} & \frac{F_{\theta_2,\theta_2}}{M_2} & \frac{F_{\theta_2,\varphi_2}}{M_2} \end{pmatrix} - \gamma \begin{pmatrix} -\sin\theta_1 F_{\theta_1,\theta_1} & -\sin\theta_1 F_{\theta_1,\varphi_1} & -\sin\theta_1 F_{\theta_1,\theta_2} & -\sin\theta_1 F_{\theta_1,\varphi_2} \\ \frac{F_{\varphi_1,\theta_1}}{\sin\theta_1} & \frac{F_{\varphi_1,\varphi_1}}{\sin\theta_1} & \frac{F_{\varphi_1,\theta_2}}{\sin\theta_1} & \frac{F_{\varphi_1,\varphi_2}}{\sin\theta_1} \\ -\sin\theta_2 F_{\theta_2,\theta_1} & -\sin\theta_2 F_{\theta_2,\varphi_1} & -\sin\theta_2 F_{\theta_2,\theta_2} & -\sin\theta_2 F_{\theta_2,\varphi_2} \\ \frac{F_{\varphi_2,\theta_1}}{\sin\theta_2} & \frac{F_{\varphi_2,\varphi_1}}{\sin\theta_2} & \frac{F_{\varphi_2,\theta_2}}{\sin\theta_2} & \frac{F_{\varphi_2,\varphi_2}}{\sin\theta_2} \end{pmatrix} \begin{pmatrix} \theta_1 \\ \varphi_1 \\ \theta_2 \\ \varphi_2 \end{pmatrix}. \quad (22)$$

Here, both θ_α and φ_α are the equilibrium values (ob-

tained as explained in the previous section). Besides,

the derivatives are evaluated in the corresponding equilibrium values. Note that here we use a 3D orientation for the magnetization vectors for convenience. The 2D choice that we made in the previous section allowed us to derive some analytical expression whereas here we will resort to numerical solutions.

The resonance frequency, Ω is derived by seeking oscillatory solutions of the form:

$$\theta_\alpha = \delta\theta_\alpha e^{i\Omega t}, \quad (23a)$$

$$\varphi_\alpha = \delta\varphi_\alpha e^{i\Omega t}. \quad (23b)$$

Substituting these expressions into Eq. (22), we obtain a linear equation system for Ω that is amenable to numerical solution. Among the four solutions, two correspond to the normal modes of each sublattice, indicating that for each sublattice, two frequencies describe the motion of θ_α and φ_α .

To calculate these resonant frequencies, we set $\gamma = 0$, i.e., focusing solely on Hamiltonian dynamics. While there is generally a dependence on the dissipation strength, it is marginal. In Fig. (S15), we present several numerical examples to illustrate the dependence of Ω on the angle ψ , which is crucial for understanding experimental outcomes. Specifically, in panel S15a, we plot the angle dependence of the non-vanishing resonant frequency as a function of the field for different anisotropy orientations, ψ . The resonant frequencies are found to follow:

$$\Omega = \sqrt{\bar{B}^2 - 2J^2\epsilon(\sin\psi - \cos\psi)}, \quad (24)$$

where $\bar{B} = g\mu_B B$. For angles less than $\pi/4$, grey dashed lines show the expected frequency curve absent a spin-flop transition. Orientations with complementary angles ($\psi_1 + \psi_2 = \pi/2$) exhibit identical resonant frequencies at zero field. The black dashed line denotes the magnetic field value for which panel S15b is simulated, corresponding to the experimental and simulation data presented in Fig. 3 in main text. Below the Néel temperature (T_N), magnetic correlations lead to distinct resonant frequencies for each anisotropy orientation, resulting in a distribution where larger angles, i.e., orientations closer to the magnetic field direction, exhibit higher frequencies.

Additionally, the variation in resonance frequency due to magnetic correlations necessitates estimating the line width (losses). Incorporating the dissipation component, which is the second line in Eq. (22), and considering the exponential decay in oscillatory solutions:

$$\theta_\alpha = \delta\theta_\alpha e^{i\Omega t - \gamma t}, \quad (25a)$$

$$\varphi_\alpha = \delta\varphi_\alpha e^{i\Omega t - \gamma t}, \quad (25b)$$

Moreover, numerical analyses suggest the approximation:

$$\gamma \propto JM_\alpha^2. \quad (26)$$

Thus, the line width increases below T_N . Although this does not determine the experimental broadening, which

is due to the fact that anisotropy introduces a distribution of resonance frequencies when spin waves emerge, as explained in the main text.

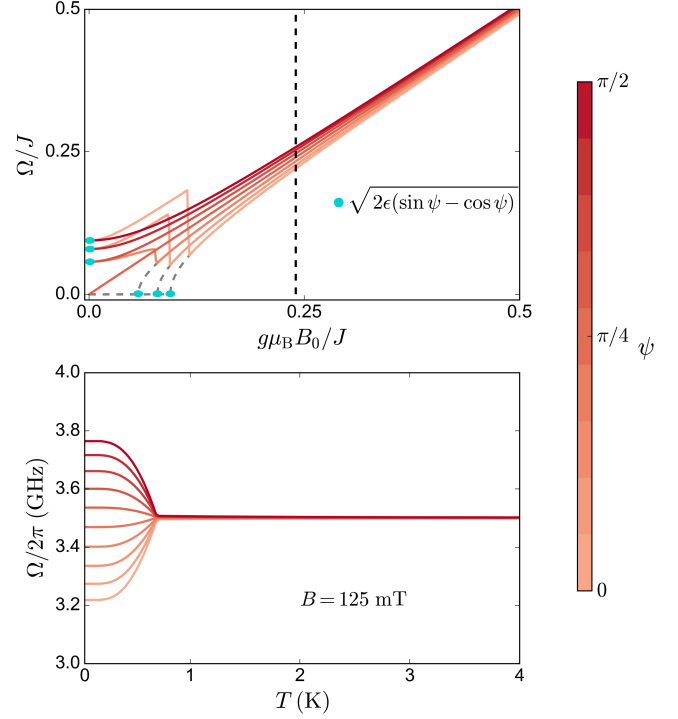


FIG. S15. **Resonant frequency of the chains according to its orientation.** In a) we show the dependence of Ω at $T = 0$ with the anisotropy orientation, ψ . We find that Ω follows Eq. (24) so angles between 0 and $\pi/4$ would follow the grey dashed line if they did not pass through the particular spin flop transition described. The black dashed line indicates the magnetic field at which the results in panel b) were obtained. There, the temperature behaviour of the frequencies for each orientation ψ is shown. Over T_N , the system is paramagnetic and anisotropy does not play any role but below that temperature, magnetic correlations show up its strong influence on the frequencies. The parameters used were $J/k_B = 0.7$ K and $J\epsilon/k_B = -0.065$ K.

VI. WAVEGUIDE QED THEORY

The B_{rms} field is in the xz plane, that is, perpendicular to the applied field. Therefore, the photons from the guide will essentially produce spin-flips in the DPPH. Thus, the Hamiltonian for our calculations will be $\mathcal{H} = \mathcal{H}_{\text{WG}} + \mathcal{H}_{\text{I}} + \mathcal{H}_{\text{M}}$, where

$$\mathcal{H}_{\text{WG}} = \int d\omega \omega (r_\omega^\dagger r_\omega + l_\omega^\dagger l_\omega), \quad (27)$$

$$\mathcal{H}_{\text{I}} = \sum_{j,n}^N \int_{\Omega_-}^{\Omega_+} d\omega \lambda_\omega(\vec{r}_j) (\sigma_{j,n}^+ + \text{h.c.}) X(\omega). \quad (28)$$

In Eq. (27), r_ω^\dagger (l_ω^\dagger) are bosonic operators, $[r_\omega, r_{\omega'}^\dagger] = \delta(\omega - \omega')$ and $[l_\omega, l_{\omega'}^\dagger] = \delta(\omega - \omega')$. They create right (left) moving photons. Besides, in Eq. (28), $X(\omega) = (r_\omega + l_\omega) + \text{h.c.}$, λ_ω are spin-photon coupling constants and the $\sigma_{j,n}^\pm$ are Pauli spin-raising and lowering operators for the j -th DPPH molecule from the n -th chain. The angle θ stands for the orientation of the magnetic field \vec{B}_{rms} generated by the waveguide at the position of the given molecule. The actual value of the coupling is given by,

$$\lambda_\omega(\vec{r}_j) = \frac{gS\mu_B}{\sqrt{2\pi}} |\vec{B}_{\text{rms}}(\vec{r}_j)| \cong \lambda_\omega \quad (29)$$

with $\vec{B}_{\text{rms}}(\vec{r}_j)$ the zero-point root mean square magnetic field generated by the current fluctuations in the waveguide. The last approximation states that we neglect distance effects. Furthermore, the dependence on the x and z coordinates can be averaged out to yield an average coupling which, ultimately, must be fitted.

A. Input-output fields and scattering

For computing the transmission, we use input-output theory¹⁸

$$r_{\text{out}}(t) = r_{\text{in}}(t) - i \int_0^\infty \frac{d\omega}{\sqrt{2\pi}} e^{-i\omega t} \lambda_\omega \int_{-\infty}^\infty d\tau e^{+i\omega\tau} \sigma_x(\tau) \quad (30)$$

With right *input* photon fields

$$r_{\text{in}}(t) := \int_0^\infty \frac{d\omega}{\sqrt{2\pi}} r_\omega(t_0) e^{-i\omega(t-t_0)}, \quad (31)$$

and the *output* ones,

$$r_{\text{out}}(t) := \int_0^\infty \frac{d\omega}{\sqrt{2\pi}} r_\omega(t_f) e^{-i\omega(t-t_f)} \quad (32)$$

and identical relations for the left fields.

1. Input fields and temperature effects

We must consider the effect of temperature. The line-molecules are thermalized at temperature T . Then, we *inject* a current, that in the case of our experiment is equivalent to a coherent state. Therefore the input field can be written as,

$$\varrho_{\text{in}} = \mathcal{A} \varrho_\beta \mathcal{A}^\dagger, \quad (33)$$

with \mathcal{A} the generator of coherent states,

$$\mathcal{A} = \sum_j \phi_j e^{\alpha_j a_j^\dagger - \alpha_j^* a_j}. \quad (34)$$

2. Transmission and reflection formulas

In the limit $\alpha \rightarrow 0$ (cf. Eq. (34)), the transmission is given by:

$$t^{(1)}(\omega) = \lim_{\alpha \rightarrow 0} \frac{\langle \alpha_\omega | r_{\text{out}}(t) | \alpha_\omega \rangle}{\langle \alpha_\omega | r_{\text{in}}(t) | \alpha_\omega \rangle}, \quad (35)$$

where $|\alpha_\omega\rangle = \exp(\alpha r_{\text{in}}^\dagger(\omega) - \text{H.c.}) |\Omega\rangle$, with $r_{\text{in}}^\dagger(\omega)$ being the Fourier transform of $r_{\text{in}}^\dagger(t)$. It is crucial to note that, in this limit ($\alpha \rightarrow 0$), the transmission is equivalent to the case of single-photon scattering.¹⁹ The superscript $t^{(1)}$ denotes that we are considering the single molecule scenario. A single molecule can be treated as a point-like object, leading to the continuity of the photon wavepacket at the interaction point with the molecule and the guide, as expressed by:

$$r^{(1)}(\omega) = t^{(1)}(\omega) - 1. \quad (36)$$

For the calculation of transmission (Eq. (35)), we refer to Eq. (30). The two-level system (TLS) dynamics are described by the master equation:

$$\begin{aligned} \frac{d\varrho}{dt} = & -i[\mathcal{H}_s, \varrho] - i\alpha \sqrt{\frac{d\omega}{dk}} g(\omega_0) \cos(\omega_0 t) [\sigma_x, \varrho] \\ & + 2\gamma(\Omega) \left(\sigma^- \varrho \sigma^+ - \frac{1}{2} \{ \sigma^+ \sigma^-, \varrho \} \right) \\ & + 2\gamma(\Omega) e^{-\beta\Omega} \left(\sigma^- \varrho \sigma^+ - \frac{1}{2} \{ \sigma^+ \sigma^-, \varrho \} \right) \\ & + \gamma_\phi \left(\sigma^+ \sigma^- \varrho \sigma^+ \sigma^- - \frac{1}{2} \{ \sigma^+ \sigma^-, \varrho \} \right). \end{aligned} \quad (37)$$

Here,

$$\mathcal{H}_s = \Omega \sigma^+ \sigma^-, \quad \Omega \equiv g\mu_B B \quad (38)$$

and γ represents the temperature-dependent rates for the spins, including both the coupling to the line and any intrinsic loss mechanisms within the molecules:

$$\gamma(\Omega) = (\xi + 2\pi\lambda_\Omega^2) (n_\Omega + 1), \quad (39)$$

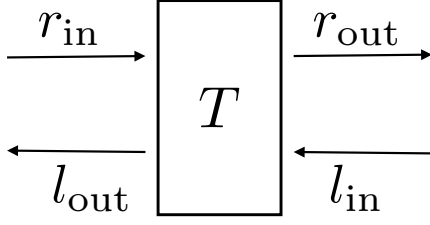
with $n_\Omega = 1/(e^{\beta\Omega} + 1)$ being the Bose occupation number, and ξ accounting for intrinsic loss mechanisms. Additionally, γ_ϕ quantifies the pure dephasing terms. The factor of 2 in front of the summation is because the master equation is coupled to both left (l_ω) and right (r_ω) modes. Solving the master equation within the linear response theory (LRT), we derive:

$$t^{(1)}(\omega) = 1 - \frac{2\pi\lambda_\omega^2 \langle \sigma_z \rangle_\beta}{\Gamma + i(\Omega - \omega)}, \quad (40)$$

where

$$\langle \sigma_z \rangle = \tanh\left(\frac{\beta\omega}{2}\right), \quad (41)$$

$$\Gamma = \lambda(\Omega) + \gamma_\phi. \quad (42)$$

FIG. S16. Graphical representation of the transfer matrix, T .

It is essential to highlight that the transfer matrix, which describes the relationship between the photon wavepacket on both sides of the molecule (refer to Fig. S16), can be expressed in terms of the transmission and reflection coefficients as follows:

$$T = \begin{pmatrix} t - r^2/t & r/t \\ -r/t & 1/t \end{pmatrix}. \quad (43)$$

Using Eq. (36), the transmission for a single molecule can be succinctly expressed as:

$$T^{(1)} = 1 + \frac{r^{(1)}}{t^{(1)}} (\sigma_x + i\sigma_y). \quad (44)$$

To prevent any misunderstanding, it is worth emphasizing that the Pauli matrices mentioned above do not pertain to those representing $1/2$ -spins. In this context, they serve merely as a convenient method for representing a 2×2 matrix.

B. Transmission in the paramagnetic phase

In the paramagnetic phase, the molecules act as independent emitters. Consequently, the total transfer matrix is determined by the product of individual matrices,

$$T = \prod_j T_j^{(1)} = 1 + \sum_j \frac{r_j^{(1)}}{t_j^{(1)}} (\sigma_x + i\sigma_y), \quad (45)$$

leveraging the property of the Pauli matrices,

$$(\sigma_x + i\sigma_y)^2 = 0. \quad (46)$$

It should be noted that the total transmission is found as [cf. Eq. (43)],

$$t_{\text{total}} = \frac{1}{1 + \sum_j \frac{r_j^{(1)}}{t_j^{(1)}}}. \quad (47)$$

By employing Eqs. (40) and (36), and recognizing that $\lambda_\omega \ll \Gamma$ in Eq. (42), we find that

$$\frac{r_j^{(1)}}{t_j^{(1)}} \approx \frac{2\pi\lambda_\omega^2 \langle \sigma_z \rangle}{-\Gamma + i\delta} \Rightarrow \sum_j \frac{r_j^{(1)}}{t_j^{(1)}} \approx \frac{N2\pi\lambda_\omega^2 \langle \sigma_z \rangle}{-\Gamma + i\delta}, \quad (48)$$

where

$$\delta = \Omega - \omega. \quad (49)$$

Thus, under these assumptions, the transfer matrix across the ensemble behaves as though scattering were occurring through a single object, but with enhanced coupling $\sum_n g_j^2$, i.e., superradiance. In the main text, we define the collective coupling as

$$G = N2\pi\lambda_\omega^2 \langle \sigma_z \rangle \quad (50)$$

leading to

$$S_{21} = |t_{\text{total}}| = \left| \frac{1}{1 - \frac{G}{-\Gamma + i\delta}} \right|, \quad (51)$$

which is Eq. (1) in the main text.

C. Transmission below T_N

When intrinsic spin interactions become significant, DPPH molecules tend to organize into AFM 1D chains. Consequently, microwave photons no longer interact with individual emitters but with spin waves ($k = 0$) that behave as bosons. We know that transmission through a boson is given by [cf with (40)],

$$t^{(1)}(\omega) = 1 - \frac{2\pi\lambda_\omega^2}{\Gamma_{\text{SW}} + i(\Omega - \omega)}. \quad (52)$$

It is crucial to realize that, now, Γ_{SW} is not temperature-dependent, meaning that transmission does not depend on temperature. Furthermore, due to anisotropy, each chain possesses a distinct angle ψ , which influences its resonance frequency as we have calculated and illustrated in Figure S15. Thus, the sum over j in (51) is across chains, each with a different frequency $\Omega(\psi)$. We can replace the sum with an integral, resulting in

$$S_{21} = |t_{\text{total}}| = \left| \frac{1}{1 + \int d\psi \sin \psi \frac{\lambda_\Omega^2 N_{\text{eff}}(T_N)}{-\Gamma_{\text{SW}} + i\delta_\psi}} \right|, \quad (53)$$

with $\Gamma_{\text{SW}} \cong \Gamma(T_N)$ and $\delta_\psi = \Omega(\psi) - \omega$, which is Eq. (4) in the main text.

-
- ¹ D. E. Williams, J. Am. Chem. Soc. **88**, 5665 (1966).
- ² D. Žilić, D. Pajić, M. Jurić, K. Molčanov, B. Rakvin, P. Planinić, and K. Zadro, J. Magn. Reson. **207**, 34 (2010).
- ³ N. D. Yordanov, Appl. Magn. Reson. **10**, 339 (1996).
- ⁴ A. D. Kent, S. von Molnár, S. Gider, and D. D. Awschalom, J. Appl. Phys. **76**, 6656 (1994).
- ⁵ H. Ohya-Nishiguchi, Bull. Chem. Soc. Jpn. **52**, 3480 (1979).
- ⁶ T. Fujito, Bull. Chem. Soc. Jpn. **54**, 3110 (1981).
- ⁷ G. R. Stewart, Rev. Sci. Instrum. **54**, 1 (1983).
- ⁸ H. Blöte, Physica B+C **79**, 427 (1975).
- ⁹ J. H. V. Vleck, Phys. Rev. **74**, 1168 (1948).
- ¹⁰ P. W. Anderson and P. R. Weiss, Rev. Mod. Phys. **25**, 269 (1953).
- ¹¹ I. Gimeno, W. Kersten, M. C. Pallarés, P. Hermosilla, M. J. Martínez-Pérez, M. D. Jenkins, A. Angerer, C. Sánchez-Azqueta, D. Zueco, J. Majer, A. Lostao, and F. Luis, ACS Nano **14**, 8707 (2020).
- ¹² T. Hümmer, F. J. García-Vidal, L. Martín-Moreno, and D. Zueco, Phys. Rev. B **87**, 115419 (2013).
- ¹³ A. Ghirri, C. Bonizzoni, F. Troiani, N. Buccheri, L. Beverina, A. Cassinese, and M. Affronte, Phys. Rev. A **93**, 063855 (2016).
- ¹⁴ M. Mergenthaler, J. Liu, J. J. Le Roy, N. Ares, A. L. Thompson, L. Bogani, F. Luis, S. J. Blundell, T. Lancaster, A. Ardavan, G. A. D. Briggs, P. J. Leek, and E. A. Laird, Phys. Rev. Lett. **119**, 147701 (2017).
- ¹⁵ J. Garcia-Palacios, J. Gong, and F. Luis, J. Phys. Condens. Matter **21**, 456006 (2009).
- ¹⁶ S. V. Vonsovskii, *Ferromagnetic resonance* (Pergamon Press, 1966).
- ¹⁷ M. P. Ross, *Spin dynamics in an antiferromagnet*, Diploma thesis, Technische Universität München (2013).
- ¹⁸ C. W. Gardiner and M. J. Collett, Phys. Rev. A **31**, 3761 (1985).
- ¹⁹ E. Sánchez-Burillo, L. Martín-Moreno, J. J. García-Ripoll, and D. Zueco, Phys. Rev. A **94**, 053814 (2016).